On Thermoelastic Impact Modelling of Frozen Composite Target During Pre – Heated Projectile Penetration Starts of Motion

JACOB NAGLER
NIRC,
Haifa, Givat Downes
ISRAEL

Abstract: - This study investigates a composite double-layer structure for improved thermal shock resistance. A modified Hugoniot elastic limit model is presented for the composite, followed by a 2D thermo-elastic impact simulation using commercial software. The simulation focuses on a composite material under initial extreme low temperature conditions with alternating metallic (Steel, Aluminum) and non-metallic layers (Kevlar 49, Graphite). The frozen target is subjected to pre- heated projectile. The objective is to optimize the composite's durability by strategically placing reinforcement particles within specific layers. The analysis explores the effect of different particle types (oil, water, Aluminum, Steel) and sizes (0.3mm, 0.5mm, 1mm) on the composite's stress response. It was found that aluminum and steel particles significantly reduce stress compared to fluid/gas particles, confirmed qualitatively by literature. Kevlar particles within the SiCp layer enhance its resistance, while Aluminum particles within the Kevlar layer offer weight reduction benefits. Moreover, for Kevlar, larger particles improve resistance, and vice versa for the SiCp case. Considering weight, a particle size of 0.5mm is chosen for both layers. Moreover, a finite element analysis of the optimized composite model subjected to thermo-elastic impact loading demonstrates its superior performance compared to the non-reinforced composite. Specific layer combinations (SiCp with Kevlar particles, Graphite or Kevlar with Aluminum particles) show the most significant stress reduction. Finally, separate 3D ballistic analysis was performed for Tungsten having 600m/sec projectile into 5 layered target with thickness of 2.8mm each layer and appropriate interaction friction (SiCp - Steel 304 - Al 7075-T651 - Kevlar 49 - Graphite Crystalline) during penetration time of 0.006sec at 300K. The dynamic explicit transient analysis was confirmed with the predecessors' analytic calculations.

Key-Words: analytic model, FEM, thermal shock, thermo-mechanical loading, suspended particles, thermoelastic response, composite material, initial frozen target, pre heated projectile, 3D dynamic explicit ballistic model.

1 Introduction

Thermal shock happens when a material undergoes a rapid temperature change, stressing the material. A material's ability to handle this stress is called thermal shock resistance. Thermal shock can be affected by many factors including the material's properties, how quickly the temperature changes, and the shape of the object. The entire process is temporary and depends on how fast the temperature changes.

The importance of protective components or elements (PCs, PEs) with variable material properties to withstand high temperatures and pressure, known as thermo-mechanical shock created in short time duration, as consequently thermo-mechanical stresses are being developed, is meaningful for mechanical, medical, environmental and civil engineering industries [1] – [66].

Initially, PCs were designed for specific limited range values of temperatures or heat fluxes. In further development stages PCs were designed to absorb high amount of energy through smart decorative layers management. The shield, actually become a protective system to withstand variety high thermal stresses, and to keep durability for reuse purposes. Those protective systems were investigated over the decades, for instance, light weight foam carbon-

Jacob Nagler

based materials combined with high thermal conductivity Graphite foam creating phase change through pores of foam has been proposed by Klett and Conway [1]. Xie *et al*. [2] have also investigated the micropores effect on photothermal anti-icing and deicing process through carbon-based photothermal superhydrophobic thermal insulation. They [2] showed that the microholes array structure can increase light absorption and hydrophobicity, including the inhibiting of the heat transfer from the surface to the subcooled substrate, which synergistically enhances significantly the photothermal conversion.

In 2013, Hu *et al*. [3] have interlaced Hollow glass microsphere (HGM) in silicon rubber (SR) matrix due to their excellent heat isolation property and light density features. Their study involved with the percentage of broken HGM effect on the overall composite shield properties (increasing of mechanical, density and thermal conductivity properties alongside of broken HGM increase was found). The current study examines pores filled with different gas or fluid materials, simulated as shell particles containing gas or fluid materials.

To understand, particularly, the effects of nanofluids over thermo-physical properties, i.e., thermal conductivity and viscosity, that have significant influence over heat transfer coefficients in case of single- or two-phase flow, one should read the study be Azmi *et al*. [4]. Accordingly, here the nanofluids will be integrated inside the pores, while their effect will be examined. Yet, viscosity will not be considered in the current essay since the fluid will be assumed as a bulk.

Other studies concerning hollow microspheres (HM) particles combination made of different materials like ceramic, silica, and glass-filled silicone rubber (SR) composites performed by Zhao *et al*. [5]. The effect of different hollow microspheres (HM) on the mechanical and thermal properties of styrene-butadiene rubber (SR) composites was investigated [5]. They found [5] that hybrid HM can effectively improve the thermal insulation property of HM/SR composites because of higher modulus of hybrid HM than the SR matrix. The hardness of composites increases with increasing single HM loading, but decreases slightly at high filler loadings due to the saturation of high modulus microspheres. The tensile strength of composites is affected by the strength of matrix, interfacial compatibility,

shape, and dispersion of particles. Also, HM, HCM and HSM effect on interfacial compatibility and optimal proportions was investigated and well elaborated alongside extensive comparisons, as well [5].

The case of 2D-asymmetric circular adjacent particles, named pebble beds inside emulsion has been investigated in the context of heat conduction, by Liu *et al*. [6], using discrete – element and finite-element method. Verified by experiments, obtained results have accurately predicted bed particle internal and external distribution of temperature due to its counterpart's particles.

Solid / Liquid phase change inside pores and cavities, particular analytical examination has been demonstrated by [7] – [8] in the context of molding and thermal protection supersonic cruise, respectively. Another example is based on polymer layered silicate nanocomposites to improve flammability resistance of heat shields against ablation by improving the effective thermal diffusivity property by Kokabi and Bahramian [9]. In their studies the researchers have not considered pores or material phase change in their examination. Although the current paper discussion is limited to pre-ablation heat transfer that resulted by thermo-mechanical impact process.

Cryogenic layered materials, consisting of several functional layers including aerogel that suitable for thermal insulation purposes under extreme conditions and nonvacuum applications was proposed by Fesmire [10]. The protective system [10] is based on layer-pairs working in combination, while each layer pair is comprised of a primary insulation layer and a compressible radiant barrier layer.

Wang *et al*. [11] reported on of carbonaceous composite materials mixtures and matrices for different heat protective applications (among them heat exchangers and space radiators). Other types of protective composite systems against ultra-high temperatures include Zirconium-doped hybrid composites as reported by [12]. They also modified thermal shock resistance coefficient to be dependent on Young's modulus and fracture strength by increasing the critical temperature difference of rupture to some extent, while claiming that their Zirconium-based ceramics coating could absorb the heat shock (suitable for nose-tip and nozzle as well as other exposed surfaces, like wings leading edge).

Jacob Nagler

Multilayer protection systems with various systematic layering methods have been proposed by Xue *et al*. [13] (in the context of Multi-laminar aligned silicone rubber (SR) flexible hybrids (SABE) with highly oriented and dispersed boron nitride (BN) and expanded graphite (EG) filler network), Zhang *et al*. [14] in the context of ramjet combustion chamber design made of internal C/C-SiC layer / first mid layer of carbon-phenolic / second mid layer aerogels / outer metal layer, Renard and Puskarz [15] in the context of firefighters protection cloth examined (by FEM) configuration based on various woven and non-woven textiles layers assemblies, respectively. Guo *et al*. [16] has recently extended the woven fabric composite shield analysis by using inverse methods based on particle swarm optimization algorithm.

Other types of protective shields based on multiphase functional phases have been suggested by Zang *et al*. [17]. He examined empirically the synergistic effect between three different functional phases of thermal insulation, i.e., hollow ceramic microspheres (HCMs), hollow silica microspheres (HSMs), and hydroxyl silicone oil blowing agent, to prepare a flexible and efficient thermal insulation composite with low thermal conductivity and high structural strength. Metamaterials are also being modified and examined to create thermal protection that is robustly and can be fast printing production [18]. Macak *et al*. [19] have predicted analytically the thermal radiation heat fluxes inside heterogeneous granular media over protective graphite tube containing pebble bed filled and nitrogen which is also can be considered as phase transition for protective shield future applications.

Impact generates stress and displacement waves in both projectile and target [20]. Traditional modeling used equations and material properties to predict stress and displacement [21]-[23]. Finite element methods (FEM) are used for advanced simulations. The initial shock wave and its effect on the projectile are of particular interest [24]-[26]. Different materials and projectile shapes can influence the non-linear process [27] - [31]. This study proposes a thermo-mechanical analytic pulse model to analyze the initial shock wave [32] – [33]. The current model considers separation of energy into thermal and mechanical components with composite material

parameters to assess shield resistance and improve armor design.

The discussion in the current work is limited to shock-based thermoelastic analysis, which is a pre-ablative analysis without chemical change of the material itself during the passage of heat and / or mechanical loads, yet, focused on strength analysis without chemical ablation phenomenon. Here, the projectile (i.e. bullet) is pre- heated to over seven hundred Celsius degrees while the target is in initial extremely frozen conditions (-248.15^0C). The idea is to observe clearly compression and tensile stress wave during process and to examine the pre heated projectile effect.

The discussion is an extension of the previous study [34], while here we concentrate on the resultant impact (principal) stress over a composite target plate through thermoelastic shock mechanism. The medium, which is the thickness of the base plate, is significant for the passage of shock waves, as we will argue later, and certainly also for continuous material change in a full ablative process. We would like to keep away from the process a change / plasticity of the ablative material as much as possible, in such a way that the target plate will *damp* the thermoplastic wave optimally before the transition to plasticity (change of material, thermoplastic waves). Two-dimensional (2D) analysis includes the impact sensitivity of target composite material (layered with and without particles), strength, temperature and size geometry. Usually, the projectile temperature is maximum 90^0C and the penetration occur in standard environmental conditions of 25^0C [35] – [36] (e.g. the maximum temperature difference will be $\Delta T \sim 65 - 75^0C$). Afterwards, the optimized shield will be examined for full elastic-plastic penetration of 600 *m*/*sec* bullet under standard 25^0C temperature conditions.

The empirical existing literature mentioned here focus mainly on double layered metal – composite rigid plates. In 1969, Wilkins *et al*. [37] have conducted study on multi-layer AD85 Alumina protective armor made of different (mainly brittle) ceramics materials (e.g. TiC, Al_2O_3, SiC, AD85, B_4C, etc.) bonded to Al 6061T6 to investigate strength and durability during impact and projectile penetration moving at about 700 *m*/*sec*. According to the researchers [37] ductility material property and gradation should be considered for armor design. New materials should be developed focusing on ceramic-metal composites

(cermets) containing less than 10% metal. Also, more focus on understanding how the metal and ceramic parts of cermets bond together. Lightweight materials like boron and beryllium compounds should be investigated. Optimizing fiber strength and elasticity in fiberglass composites is recommended. In 1997, Espinosa *et al*. [38] have led numerical investigation of ballistic penetration into multilayered structural systems based on multiple plane micro - cracking model. Two types of ceramics have been considered for each shield test, i.e., Alumina (Al_2O_3) and SiC while the cover plate was made from RHA steel. Another type of target made of alternate layers of aluminum and PMMA layered materials composition was investigated. The projectile normal impact velocity was 1500 *m/sec*. Their main contribution was that they have found that the design of the layers (material choice and arrangement) is more important than the specific type of ceramic used. Next, Kanel *et al*. [39] focused on the complex response of brittle materials (ceramics, glasses, rocks) under dynamic compressive loads (explosions, impacts). Unlike tensile loading, where these materials shatter easily, compressive behavior is less understood, especially at high strain rates and hence, challenges in understanding and predicting *how brittle materials respond under rapid compressive loads* still exist. Their key findings include:

- **Interpreting failure is difficult:** Traditional methods (Hugoniot data, shock wave profiles) are not sufficient to distinguish between brittle (cracking) and ductile (deformation) failure.
- **Spall strength can be misleading:** Material may still be ductile even with reduced shear strength if spall strength (resistance to tensile failure) is not zero.
- **Failure mode depends on stress state:** Cracks may form under high compressive stress even if unloading shows some tensile stress. Observing a failure wave is a clear sign of brittle response.
- **Cracking vs. plastic slip:** Inelastic deformation can occur through cracking or slippage within the material. Confining pressure can suppress cracking and promote ductility.

- **Strain rate matters:** High strain rates can make material behavior more sensitive to microscopic processes.
- **Griffith's criterion for dynamic failure:** This approach seems to better predict failure mode (brittle or ductile) under dynamic compression compared to yield criteria used for ductile metals.

Overall, the study highlights the challenges in understanding and predicting how brittle materials respond under rapid compressive loads.

Alternatively, Candera and Chen [40] – [41] investigated the complex impact response of layered composite materials, like those used in armor. Unlike metals and ceramics, the stress waves in composites are irregular due to the layered structure. They developed an analytical solution to predict the stress response within a layered composite under impact, considering material properties and layer thickness factors. Their study confirms that material heterogeneity at the interfaces between layers is the main reason for the observed complex stress wave profiles for thin layered plates (most effectively) and suggested it can be used for designing optimal layered armor. The study acknowledges limitations of the model for thicker plates and complex 2D woven composites, recommending further research in these areas. In continually, Chen *et al*. [42] investigated the wave structure in composite materials under high velocity impact loading. They claimed that homogenization methods, effective for low velocity impacts, are not suitable for this scenario. An analytical solution was presented for layered composites under high velocity impact, applicable in elastic cases with extensions proposed for shock regimes. The analysis assumes perfectly bonded interfaces and damage-free constituents. Three key heterogeneity factors influencing the material response were identified:

- Impedance mismatch: Affects reflection/transmission ratios, stress wave structure, and wave arrival time.
- Interface density: Determines wave train strength and oscillation frequency. High density leads to shorter rise time and higher frequency (shock regime: overtaking effect).

- Thickness ratio: Governs wave propagation patterns, affecting rise time, oscillation behavior, and mean stress. Explains the anomaly of lower measured wave speed compared to constituents.

Overall, their study [42] provided valuable insights into the wave behavior of composite materials under high velocity impact loading.

Colombo et al. [43] explored a new lightweight bulletproof, vehicle armor or any other blast protection armor design. Their design combined for the first-time ceramic tiles with a special ceramic foam infiltrated with polymer to create a lightweight ballistic protection system, which also absorbs effectively and dissipate energy from impacts. Due to their successful test results, armor made with this design could stop fragmentations (e.g. bullet calibers) using a thinner ceramic tile (lighter weight) compared to traditional methods. Rajendran et al. [44] used a modified two-cap constitutive model to simulate shock wave propagation in powdered ceramics under impact loading. Their model was validated with experimental data and successfully captured the effects of factors like shock intensity, material impedance, and densification on the shock wave behavior, as consequently, providing valuable insights into the complex behavior of powdered ceramics under shock loading, which is difficult to obtain experimentally. The findings can be used to improve constitutive models for predicting damage in ceramic armor plates. The problem of composite materials thickness effect when struck by objects at high speeds (impact, damage, and penetration) have been examined by Gama and Gillespie Jr. [45]. They accomplished it using a computer simulation technique called explicit finite element analysis (FEA). The model accurately predicts how the material will break and how far the object will penetrate at various speeds (validated with experiments). Two main penetration phases are identified: short-time shock compression and long-time penetration. The model can be used to design composite materials that absorb more impact energy.

Specifically, Babei et al. [46] investigated how the order and type of materials in a double-layered target affect its resistance to being penetrated by a projectile. They tested four configurations: aluminum-aluminum, aluminum-steel, steel-aluminum, and steel-steel. Steel-steel offered the highest resistance, followed by steel-aluminum, aluminum-steel, and then aluminum-aluminum. The study also successfully developed a computer model to simulate these impacts, achieving good accuracy. The model showed that the order of materials matters, with steel absorbing more energy when placed in the front layer compared to aluminum. A previously existing analytical model (Ipson and Recht) did not accurately predict the impact resistance for aluminum-steel and steel-aluminum targets. Another study by Shanel and Spaniel [47] have explored using computer modelling to design lighter, composite armor for vehicles. They fired real bullets at armor plates and compared the damage to computer simulations. By adjusting the model, they achieved good agreement with reality. This validated model can now be used to design composite armor without needing as many real-world tests. This is important because composite armor is lighter than traditional metal armor, which can improve vehicle performance. Islam et al. [48] study addresses the challenge of simulating how ceramic and ceramic-metal plates react to high-speed impacts from metal rods. They developed a computer model to analyze these impacts, whilst testing different material models for the ceramic and found that the JHB model produced the most accurate results compared to real-world experiments. Their model can predict various damage forms in the plates, including cracks, fragmentation, and bending. Peimaei and Khademian [49] examined how adding silicon carbide (SiCp) to aluminum plates (Al7075) affects their ability to stop a projectile (bullet) using FEA. They found that plates with more SiCp (9%) absorbed more energy and stopped the bullet completely, while those with less SiCp (3% and 6%) absorbed less energy and did not stop the projectile (bullet) entirely. The study also explains the mechanics of how the bullet interacts with the plate and how the damage zone increases with more SiCp. Fernando et al. [50] have proposed a new design for armor using a layered metal system (impedance-graded multi-metallic or IGMM) to absorb the impact of high-speed projectiles. The IGMM system uses metals arranged in a specific order to weaken and reduce shockwaves. The research showed that IGMM targets were effective at reducing stress on

impact and preventing metal spalling compared to traditional monolithic targets. Ranaweera *et al*. [51] addresses a gap in knowledge regarding multi-metal layered armor (MMMLS). While traditionally, heavy steel plates have been used, they are impractical for lightweight applications. MMMLS offers a solution but research on it is scattered and lacks consensus on the best design. Their study reviewed the effects of various factors on MMMLS performance, including metal types, thickness, plate arrangement, and connection methods. They found that steel-aluminum combinations were most common, but the optimal plate order is unclear. An interesting new concept, impedance-graded systems, needs further exploration. The study proposes several avenues for future research:

- Including new metals like titanium and exploring their alloys with steel.
- Investigating the impact of increasing MMMLS layers beyond double- and triple-layered systems.
- Validating the impedance mismatch concept for optimal ballistic performance.
- Exploring alternative connection methods between metal layers.
- Researching continuous MMMLS manufacturing techniques like explosive welding and 3D printing.
- Comparing the ballistic performance of continuous vs. discontinuous MMMLS designs.

Overall, this study highlights the need for further research to optimize MMMLS design for superior ballistic protection while maintaining a lightweight construction.

Goda and Girardot [52] investigated the ballistic performance of ceramic/composite armor using computer simulations. They created impact simulation durability of a ceramic plate backed by a composite layer against moving projectile. The ceramic layer stops the bullet initially, then shatters. The composite layer catches the fragments and absorbs energy. The study also showed the ceramic and composite layers interaction affects the armor functionality. Their model can help design better armor by predicting how different materials and designs will perform. In similar way, Jasra and Saxena [53] examined

how the pre-stressed state of a material (tensile or compressive stress) affects its fracture behavior under high-speed impact. They created a computer model to simulate a blunt projectile hitting a flat steel plate under various pre-stress conditions. The model showed that pre-stress significantly affects how the plate fractures. Tensile pre-stress improves the plate's ballistic performance (resistance to penetration) by reducing damage accumulation. Compressive pre-stress weakens the plate and makes it easier to penetrate. It might be significant to real-world structures experience residual stress from welding or other processes (i.e. high-velocity impacts resistance), which can act like pre-stress.

Current essay presents a modified equation of the approximate Huogoniot elastic limit [34], [54] – [59] which basically corresponds through equation algebraic shape for two kinds of developed stress type inside rigid solid materials (i.e. especially, ceramics, metals); spall strength (σ_{spall}) and elastic strength (σ_{HEL}), respectively. The point on the shock wave at which a material transitions from a purely elastic state to an elastic-plastic state is called the Hugoniot elastic limit (HEL) as illustrated in Fig. 1. The Hugoniot elastic limit is derived from the equation of state (EOS) [54] – [55], a thermodynamic relationship between pressure, density and temperature parameters through mass, momentum and energy conservation equations. The HEL approximation stress is:

$$\sigma_{HEL} = \frac{1}{2} U_H \rho_0 C_l \qquad (1)$$

where the free surface velocity (projectile impact velocity), bulk longitudinal speed and density represent by U_H, ρ_0, C_l, respectively. The spall strength represents the reflection of the initial compression pulse from the free surface that generates tensile stresses. Spalling is initiated when stress reaches the fracture threshold as illustrated in Fig. 1. Afterwards, tensile stresses relax to zero as the fracture develops. As a result, a compression 'spall pulse' wave appears in the extended material free surface velocity profile [56] and accompanied with decaying velocity oscillations due to subsequent wave reflections between the sample surface and the fracture surface. The spall strength [54] is characterized

Jacob Nagler

by shorter load duration while the drop in surface velocity from the peak value (U_f) to the onset of spallation-the so-called "pullback''($\Delta U_{fs} = U_f - U_m$, U_m is the free surface velocity just a head of the spall pulse) - is proportional to the tensile stress in the spall plane [57] – [58]:

$$\sigma_{spall} = \frac{1}{2}\Delta U_{fs}\rho_0 C_{bulk} \qquad (2)$$

where the bulk sound speed and density represent by ρ_0, C_{bulk}, respectively. The $C_{bulk} = \sqrt{K(1-v)/\rho(1+v)(1-2v)}$ sound speed [59] is dependent on the bulk modulus K while the longitudinal sound speed $C_l = V_e = \sqrt{E(1-v)/\rho(1+v)(1-2v)}$ is dependent on the Elastic Young's modulus (E). Both dependent on the bulk's Poisson's ratio and the material density.

However, here we are interested in the purely elastic state of material's limit, since the idea is to delay the plastic transition as much as possible, and to extend the elastic domain both in terms of the amplitude of the maximum allowable elastic yield stress and the elastic flexibility behavior (i.e. high elastic straining). As consequently, the discussion will focus on the modified approximated Hugoniot elastic limit (HEL) as brought by Nagler [34]:

$$\sigma_{modified-HEL} = \frac{1}{2}U_H\rho_0 C_l - \rho_0 C_p \Delta T = \frac{\rho}{2}V_{impact}\left(V_e - V_{impact}\right) \qquad (3)$$

where $V_{impact} = U_H$, $V_e = C_l$ and ΔT, C_p are the projectile's impact temperature difference at the initial contact and material's heat capacity, respectively. In the following sections 2 -3 we will introduce algebraic procedure for the composite (mainly, double) rigid layer case accommodation alongside experimental validation, respectively.

Remark that alternative analytic strength equation is proposed by [12], [60] – [62]. The mentioned method is based on the following generalized double layer UHTC (Ultra-high temperature ceramics) impact stress due to surficial thermal shock:

$$\sigma_{UHTC} = \frac{E_B E_C[T]\alpha_C[T](T-T_i)}{E_B[T]\cdot(1-v_C)+E_C[T]\cdot(1-v_B)} \qquad (4)$$

where $E_B, E_C[T], \alpha_C[T], v_B, v_C, T_i$ are the base material Young's modulus, ceramics material Young's modulus dependent on temperature, Poisson's ratio of base and ceramics materials and the initial environment temperature, respectively.

From here we will pass to discuss briefly on the protective shield containing pores as appear in [63] – [66] and their effect over the protective shield, which will be also examined in the current essay continually in Sec. 4 - 5. Wei *et al.* [63] investigated how rapid temperature changes (thermal shock) damage carbon composite used in pantograph strips for electric trains. They found that Thermal shock weakens the material by increasing pore size and causing cracks. This damage gets worse with repeated heating and cooling cycles. The damage is linked to the different expansion rates of materials in the composite under temperature changes. Water trapped in the pores worsens the damage by rapidly turning to vapor during heating. Overall, the study highlights the importance of considering thermal shock resistance when designing pantograph strips for reliable performance. Ramírez-Gil *et al.* [64] proposed a new design methodology for lightweight ballistic resistant steel plates based on holes. They achieved weight reduction by creating holes in the steel plates using two approaches: parametric design based on biological structures and topology optimization. Testing showed that the topology optimized design achieved similar ballistic resistance to solid plates while being lighter, which is a significant improvement. Their study [64] is the first to explore topology optimization for designing ballistic resistant structures and paves the way for new, lighter protective gear. The study also identifies limitations, such as potential crack formation in the perforated plates and the need for more advanced manufacturing processes for mass production. Overall, this research offers a promising new approach for the ballistic protection industry using conventional materials and processes, potentially making ballistic protection more affordable and accessible. Moreover, Li *et al.* [65] examined the hollow pores potential by investigating how a metal plate that is already deformed (due to an explosion for example) will perform differently when hit by a projectile compared to a static metal plate. They found that the way the plate deformation manner

significantly affects its resistance against projectile. Also, they used a combination of experiments and simulations to explore this effect in detail. In addition, they have found that deformed plates can stop some projectiles better than static plates, but it depends on the amount of deformation and the shape of the projectile. There are three main ways that deformation affects how well a plate stops a projectile:

- o The deformation can give the plate some extra energy to resist the projectile.
- o The deformation can change how much energy the plate absorbs as it bends and stretches.
- o The deformation can change the forces acting on the projectile as it punches through the plate.

Accordingly, one can design armor that takes advantage of deformation to improve its performance, but need to consider how much deformation is helpful and how much is harmful. Wen *et al*. [66] introduced a new type of ceramic material, 9-cation porous high-entropy diboride (9PHEB), with excellent mechanical strength and thermal insulation even at high temperatures. Traditional porous ceramics struggle to be both strong and good insulators. They created 9PHEB using a special technique and it achieves both high strength and good thermal insulation at up to 50% porosity. This makes 9PHEB a promising material for extreme environments requiring thermal insulation.

Finally, examples of thermal shock space applications including penetration variations and double bumper shock shield in NASA including different situational investigation of penetrations can be found in [67] – [68], respectively. The applications of Thermal Protection System (TPS) materials, specifically Polymeric Ablatives (PAs) in the aerospace industry are numerous, based on Natali *et al*. [68]. TPS materials protect vehicles and probes during atmospheric re-entry and high-temperature environments. PAs are the most versatile type of TPS material due to their tunable density, lower cost, and high heat shock resistance compared to non-polymeric materials. Nanostructured polymeric ablatives (NPAs) show promise for improving heat resistance and reducing weight, yet, further understanding is required to optimize processing techniques and cost. The future of NPAs likely involves combining them with heat-resistant fibers to improve performance.

2 Modified Hugoniot elastic limit for composite double layer under thermal shock analytic model

Suppose we have general material protective shield specimen that is subjected to thermo-elastic impact loading as appear in Fig. 2. The exerted (input) acting force impact over the material surface yields reaction (output) force. The general kinematic and force equilibrium over a plate with acting input ($P_1(t)$) / reaction output ($P_2(t)$) forces in Cartesian coordinates that is derived by Newton's 2nd law is:

$$\bar{f} = P_2(t) - P_1(t) = m\ddot{x} + c\dot{x} + kx \quad (5)$$

where $\bar{f}$ is the force vectors, m, c, k are the total mass (specimen mass and projectile mass), specimen dumping coefficient and stiffness coefficient. x is the longitudinal dimension, denoting the elastic impact wave propagation.
Now, the force difference also fulfills the following stress equilibrium multiplied by the projectile area section A:

$$P_2(t) - P_1(t) = \sigma_{mech}A + \sigma_{thermal}A \quad (6)$$

Where the mechanical (σ_{mech}) and thermal ($\sigma_{thermal}$) stresses supply stresses supply the uniaxial strain condition where are shear stresses zero [34]:

$$\sigma_{thermal} = -\frac{E\alpha}{1-2v}\Delta T; \; \sigma_{mech} = \frac{1-v}{(1+v)(1-2v)}E\varepsilon \quad (7)$$

Note that those relations are derived from the generalized constitutive stress relation classical thermo-elastic model equilibrium. In case of rigid isotropic material with hollow pores:

$$\sigma_{impact,final} = \frac{\bar{f}}{A} = \frac{P_2(t) - P_1(t)}{A} =$$
$$\underbrace{\frac{\rho}{2}V_e V_{impact} - \rho C_p \Delta T}_{\sigma_{impact}} -$$
$$\phi \underbrace{\left(\frac{1-v}{(1+v)(1-2v)}E\varepsilon - \frac{E\alpha}{1-2v}\Delta T \right)}_{\sigma_{resistance}} =$$

$$\underbrace{\frac{\rho}{2}V_{impact}\left(V_e - V_{impact}\right)}_{\sigma_{impact}} -$$

$$\phi\left(\underbrace{\frac{1-v}{(1+v)(1-2v)}E\varepsilon - \frac{E\alpha}{1-2v}\Delta T}_{\sigma_{resistance}}\right) \quad (8)$$

where $\phi = 1 - \psi$ which is the volume fraction of the active protective material that resists the penetration of the projectile. ψ is the relative free portion (fracture) of an inactive material substance (voids, hollows, empty pores). Observation in Eq. (8), might lead to the comprehension, by substituting $\phi = 0$ into Eq. (8), we return back to the impact peak stress in the homogenous case [34].

In case we have particles or filled gas pores mixed instead of hollow / empty pores, then by superposition, Eq. (8) becomes:

$$\sigma_{final} = \sigma_{final}\big|_{\phi=1-\psi'} - \sigma'_{final}\big|_{\phi=\psi'} \quad (9)$$

Where,

$$\sigma'_{final} = \frac{1-v'}{(1+v')(1-2v')}E'\varepsilon' - \frac{E'\alpha'}{1-2v'}\Delta T \quad (10)$$

while $E', \alpha', \varepsilon', v'$ are the particles elastic properties. In case of one-dimensional multi-layer shield, then the conditions will be:

$$\begin{cases} \sigma_{in,2} = \sigma_{final,1} \\ \sigma_{in,1} = \sigma_{in} \\ \sigma_{in,i} = \sigma_{final,i-1}, i = 1:1:N; N \in \mathbb{N} \end{cases} \quad (11)$$

There is a difference in terms of the development of elastic impact stress for cases of connecting particles/pores in a continuous row or laterally, as well as the effects of spreading the spacing in a row or column. The suggested algorithm might be with the analytic / numerical

composite scheme, proved by [40] - [41], [43], [69]. In similar way to (8), we can write the classical equations for the thermo-elastic micromechanical composite lamina stress as:

$$\sigma_{impact,final} = \sigma_{fibers}\big|_{impact}\frac{A_f}{A_c} +$$

$$\sigma_{matrix}\big|_{impact}\frac{A_m}{A_c} \quad (12)$$

where $\sigma_{c,f,m}$ and $A_{c,f,m}$ are the composite stress and area of composite, fiber, and matrix, respectively. Now, $\sigma_{fibers}\big|_{impact}$ and $\sigma_{matrix}\big|_{impact}$ will supply Eq. (3), by:

$$\begin{cases} \sigma_{fibers}\big|_{impact} = \frac{\rho_{fibers}}{2}V_{impact}(V_{e,fibers}-V_{impact}) \\ \sigma_{matrix}\big|_{impact} = \frac{\rho_{fibers}}{2}V_{impact}(V_{e,matrix}-V_{impact}) \end{cases}; \quad (13)$$

Next section, target layers component under thermo-elastic loading shock will be examined from mechanical impact loading prospective instead of ballistic aspect in order to separate between the mechanical and thermal components that develops during the process at the very initial motion start (few initial microseconds). Finally, the protective shield containing particles will be also examined separately. The examination will be performed using FEM (finite element method) procedure by commercial software, focusing on internal components material's layer, connectivity, particularly, particles' material size. The investigation will consider high pressure and temperature loadings values, approximately $100\,atm$ and $726.85°C$, respectively.

3 General approximate analytic approach for energy absorption evaluation and material selection of composite shield

In order to examine the plastic aspect, we would like to obtain a sufficient initial approximation in order to estimate the deformations, strains and displacements that develop against a damage model. It should be understood *that the sensitivity* to the materials properties is ultimately derived from the behavior of the deformation in the plastic state, i.e., the damage criterion is combined with stress properties. Hence, we need that *averagely* each layer

absorbs a certain *percentage* of the energy. In each layer, we define in advance what percentage of the total energy it will absorb, then, we will get the stiffness of each layer according to a certain percentage of the total energy multiplied by the thickness of the layer and divided by the cross-sectional area of the sphere and the difference of the squared displacement to failure.

The theory will be developed based on the author previous papers [75] – [76]. Suppose we

Jacob Nagler

have general composite shield specimen as appear in Figs. 2 – 3. Now, we will consider the specimen as spring with two states: linear - elastic and non-linear plastic, such as each state represents difference spring' stiffness constant. The kinetic energy input $1/2 m_p v_p^2$ (m_p, v_p are the projectile mass and velocity, respectively) will be transferred into spring potential energy and heat losses as appear in the following energy conservative equilibrium:

$$\frac{mv^2}{2} = \int_{x_{el}}^{x_{pl}} kx dx = \frac{k_{pl}x_{pl}^2}{2} - \frac{k_{el}x_{el}^2}{2} + mC_v\Delta T \approx$$
$$\frac{k_{pl}x_{pl}^2}{2} - \frac{k_{el}x_{el}^2}{2} . \quad (14)$$

Since $mC_v\Delta T \ll \frac{k_{pl}x_{pl}^2}{2}$, where the stiffness constants (k_{el}, k_{pl} are the elastic and plastic specimen material stiffnesses, respectively) are dependent over the material states (plastic or elastic) and displacements (x_{el}, x_{pl} are the elastic and plastic relative specimen displacements, respectively). Now, using the spring force – stress balance relations, we have the Hooke's law,

$$F_{elastic} = \underbrace{E_{el}\varepsilon_{el}}_{\sigma_{linear-elastic}} A = k_{el}x_{el} , \quad (15)$$

where $E_{el}, \varepsilon_{el},$ and A are the Young' elastic modulus, elastic strain and projectile are section, respectively, whereas the power Hooke's law fulfills the plastic state stress as [77] − [78]:

$$F_{plastic} = \underbrace{C\varepsilon_{pl}^n}_{\sigma_{non-linear-plastic}} A = k_{pl}x_{pl} , \quad (16)$$

where the maximum tensile stress $C \approx 2.2E_{el}\varepsilon_{pl}$ (or the true stress where the true strain $\varepsilon_t = 1$), n - hardening index (usually in rigid metals ≈ 0.17) maximum plastic strain value, $\varepsilon_{pl}\big|_{max} = 0.2$ such as $2.2 \cdot 0.2^{0.17} \approx 1$ for hard metals and rigid parts (even though graphite and Kevlar materials stress-strain curves act differently than in metals case due to their high rigidly performance and their composition with metals, it will be considered similarly [79] − [80] as initial required Young's modulus evaluation). x_{el} and x_{pl} are defined as:

$$x_{el} = \varepsilon_{el}\big|_{max} L, \quad (17)$$
$$x_{pl} = \varepsilon_{pl}\big|_{max} L, \quad (18)$$

where L is the total layered target thickness. Therefore, since $\varepsilon_{el} = 10^{-4}$ and L is few millimeters size, then, $x_{el} = 10^{-3}$. Accordingly, the elastic potential energy expression becomes approximately zero.

$$\frac{k_{el}x_{el}^2}{2} = \frac{AE_{el}}{2}\underbrace{\varepsilon_{el}^2 L}_{\to 0} \to 0 . \quad (19)$$

By substituting back (16) and (18) − (19) relation into (14), we obtain:

$$\frac{mv^2}{2} = \frac{E_{el}A\varepsilon_{pl}\big|_{max} x_{pl}}{2} = \frac{E_{el}Ax_{pl}^2}{2L}, \quad (20)$$

where $\varepsilon_{pl}\big|_{max} = x_{pl}/L$; Assuming the projectile has cylinder geometry and since the mass constitutes a multiplicative sum of volume (V_p) and density as $m_p = \rho_p V_p$ while the volume is $V_p = AL_p$ and the projectile length is denoted by L_p, we finally obtain an approximation for the elasticity modulus as:

$$E_{el} = \frac{\rho_p L_p L v^2}{x_{pl}^2}, \quad (21)$$

where accepted literature typical values for the maximum plastic displacement are about $x_{pl} \approx 0.5 \sim 1mm$, since if the maximum strain is $\varepsilon_{pl}\big|_{max} = 0.2$ and the thickness width is about few (2.5) millimeters, then by multiplying the parameters, yields $x_{pl} \approx 0.5mm$. Remark that for different velocities the ratio between different materials is approximately equivalent to the squared velocity to plastic displacement ratio value as $E_{el} \propto (v/x_{pl})^2$. For $v = 600m/sec$, $\rho_p = 8500 [kg/m^3]$, $L_p = 70mm$, and the total sum of layers are $L = 20mm$, then the total elastic modulus equal to $E_{el,total} \approx 8 [GPa]$. In other words, the meaning is that in case of 10 homogenously layers with single layer thickness of $2mm$, averagely, where each layer absorbs the same proportional value of kinetic energy, the required averagely elastic modulus of each layer to withstand the plastic stress and deformation will be $\bar{E}_{el,single\ layer} \approx 80 [GPa]$.

In the case of impact slicing or cutting, one may insert the Young's modulus of elasticity expression (21) based on kinetic energy into the stress relations derived by Mora *et al*. [105]- [106] and Arnbjerg-Nielsen *et al*. [107] and have closed analytical explicit solution for high shear strain energy or buckling.

The transition from elastic to plastic energy is the focus of the specimen mechanical energy absorption, because in the elastic state the deformation returns to its previous state while in the plastic state it remains in its current state. In reality, it is of course necessary to perform a large number of firing tests experiments because both the speed of the projectile changes from experiment to experiment and the hitting

angle of impact. Remark, care must be taken to have a middle layer that disperses the shocks so that the wearer of the vest shield will not be damaged by the concentrated shock. It is customary to apply this layer of rubber, metallic (e.g. aluminum compound) foam or Dyneema materials. In many applications where thermal energy is involved, the thermal strain fulfill a linear relationship with temperature difference $\varepsilon_{th} = \alpha \Delta T$ (α is the thermal expansion coefficient) and therefore the total strain will be composed from the mechanical and thermal strain linear sum as $\varepsilon_{Total} = \varepsilon_{th} + \varepsilon_{mechanical}$.

Moreover, it should be understood that energy management of layers in layered systems (Laminated system kinetic energy management) is a complex thing. To illustrate, we assumed that the energy is distributed in a uniform / homogeneous way, and in any case, the Young's modulus per layer is derived from dividing by the number of layers (n). In more thoroughly way of thinking, the energy terms or terminology, when speaking in energy language, it is necessary to decide how much *energy* each layer absorbs and accordingly, the Young's modulus / coefficient of elasticity is determined. This process is carried out using multi-level *layer optimization*. Example 1: Absorption of kinetic energy:

- First layer: 40%.
- Second layer: 30%.
- Third layer: 20%.
- Fourth layer: 10%.

Example 2: Absorption of kinetic energy:

- First layer: 30%
- Second layer: 20%
- Third layer: 20%
- Fourth layer: 20%
- Fifth layer: 10%

The 'thumb rule' says that the first layers sacrifice themselves for maximum energy absorption in relative to the following layers. At the same time, sometimes we would like to have 'strong' 'weak' layers materials in terms of strength, arranged alternately, sometimes in a direction perpendicular to the fibers (0^0, 90^0, 180^0, 360^0) and sometimes from other considerations, such as heat transfer or shock dissipation. In case of extremely high energies (high kinetic energy, e.g. velocity > 600 m/sec) the required Young's modulus of each layer is high such as it is difficult to obtain materials in reality with high Young's modulus values.

Therefore, we would like the energy absorption to apply to as many layers as possible with maximum Young's modulus according to what currently exists in reality (i.e. the stock market). On the other hand, there is still room to consider as the number of existing materials have a high energy absorption capacity increasingly, to propose a different multilayer arrangement than is customary according to the discussed thumb rule. Alternative way, is to vary the thickness or to use larger strain materials with special suspended particles.

Layers with high energy absorption capacity with weak layers, alternately, for the simple reasons of weight reduction, adaptation to production capacity (like molding pressure), heat transfer, shock dispersion or cost reduction. The presented method will be used continually when concerning the full plastic projectile penetration.

The way in which the developed internal stresses are distributed when hitting the target is characterized by unique failure mode impacted plate mechanism [98] – [99], either by a bullet projectile or a hardened rigid part (metallic, other), whether dependent on the angle of the projectile impact in relation to the target [100] or the projectile head shape and obliquity incidence angle design [101] - [102], or even impact with a projectile made of soft or fine materials [103] – [107], each *perpendicular* input force (component) or pressure might be evaluated through the volumetric energy expression according to the following relationship (after making some algebraic manipulation of Eq. (5) appearing in Ref. [34]):

$$\sigma_{modified-HEL/impact} = \frac{\rho}{2} \frac{F\Delta t}{m} \left(V_e - \frac{F\Delta t}{m} \right)$$

(22)

where $V_{impact} = F\Delta t / m$ (assisting the impulse relation), Δt is the contact time difference, usually $\Delta t \sim 0.1 - 1 [\mu sec]$ [34] and the extracted (or given by empirical measurements) term of F from (22) represents the perpendicular force component acting on the target (whereas V_{impact} is given and therefore $\sigma_{modified-HEL/impact}$ using Eq. (3)), respectively. In case of distributed pressure (P) input, the perpendicular force term should only be divided by the effective impact area (A) such as $P = F/A$. The internal stresses then can be readily determined by substituting F or P loading expressions into the developed stresses

relations in the appropriate literature [98] – [99] which also suitable for high shear strain energy which suitable also for slicing or cutting applications [103] – [107]. Be reminded that the input force can be also found directly by $F = \frac{m_p V_{impact}}{\Delta t} = \frac{\rho_p}{2} V_{impact}^2 A$ with the appropriate pressure term $P \approx \frac{\rho_p}{2} V_{impact}^2$. Remark that $\sigma_{modified-HEL/impact}$ is the resulting peak stress while P is the input pressure.

4 General approximate analytic approach for energy absorption evaluation and material selection of protective ablative insulation

In the same manner as in Sec. 3, an approach to evaluate erosion (ablation) rate in protective energy applications (e.g. external or internal (liquid, solid or hybrid) rocket motor (SRM) or spaceship insulations, internal protection in nuclear core, etc.) will be introduced [82] – [85]. Indeed, the case of ablation concerns material removal or thermochemical phase change (virgin >> gas / pyrolysis >> char) while the previous section was concerning material deformation. However, since the char state occur when threshold temperature is achieved (T_{char}) and hence minimum energy balance between the external thermal gas energy and the material minimum thermal capacity energy *until prescribed threshold* char temperature is obtained could be used as follows. In other words, the problem we are trying to solve is what is the maximum distance (x_s) and the minimum time (Δt) for char state formation for a given threshold temperature to rise in order to estimate the optimal erosion rate. It is assumed in the process that the calculation is strict and maintains a linear relationship between the total relative distance of the erosion (material removal) and the speed of the erosion rate through time difference (Δt). In addition, the calculation assumes overloading region of erosion rate. Accordingly, the classical unsteady transient state energy equilibrium is:

$$m_s C_p (T_{char} - T_s) = h_c A_s (T_i - T_s) \Delta t ,$$
(23)

where the left-hand side term ($mC_p(T_{char} - T_s)$) represents the resulting thermal energy developed inside the ablative material caused the equilibrium right-hand side term, such as the

flowing gas thermal convective energy ($h_c A(T_i - T_s) \Delta t$). The parameters $A_s, C_p, T_{char}, T_\infty, T_i, h_c, m_s, \Delta t$ represent the shield apparent area for the heat entrance, ablative heat capacity, charred temperature of the protective ablative material, gas surface temperature, the environment initial temperature, the thermal convective coefficient, the ablative protective shield mass and time difference, respectively. Now, by simple algebraic manipulation, Eq. (23) becomes in the following relationship form:

$$\frac{T_{char} - T_s}{T_i - T_s} = \frac{h_c A_s \Delta t}{m_s C_p} .$$
(24)

By substituting $m_s = \rho_s V_s = \rho_s A_s x_s$ and using the erosion rate term $u_s = x_s / \Delta t$ with some algebraic manipulation, yields the expression for the erosion rate speed:

$$u_s = \frac{h_c}{\rho_s C_p} \frac{T_i - T_s}{T_{char} - T_s} ,$$
(25)

where $T_i, T_{char} < T_s$ and ρ_s, V_s, are the protective shield ablative material specimen density and volume, respectively. In this stage, we will write the convective coefficient parameter as the ratio between the heat flux (q_s) and the temperature difference ($T_i - T_s$) created over the ablative material external / outer surface, by:

$$h_c = \frac{q_s}{T_s - T_i} .$$
(26)

Substituting relation (26) back into (25) gives:

$$u_s = \frac{q_s}{\rho_s C_p (T_s - T_{char})} ,$$
(27)

and the appropriate total charred erosion distance is:

$$x_s = u_s t_s = \frac{q_s t_s}{\rho_s C_p (T_s - T_{char})} ,$$
(28)

where t_s is the total heating (e.g. burning) time. Moreover, the more generalized energy case that considers also the heat radiation, turns (23) into:

$$m_s C_p (T_{char} - T_s) = h_c A_s (T_i - T_s) \Delta t + h_r A_s (T_i^4 - T_s^4) \Delta t$$
(29)

where h_r is the total manipulation between the view factor ($F_{1 \to 2}$) and the Stefan-Boltzmann constant (σ). After similar algebraic manipulation, the radiative and convective erosion rate will have the following shape:

$$u_{s,convection \& radation} = \frac{h_c}{\rho_s C_p} \frac{T_i - T_s}{T_{char} - T_s} + \cdots + \frac{\sigma F_{1 \to 2}}{\rho_s C_p} \frac{T_i^4 - T_s^4}{T_{char} - T_s} .$$
(30)

Illustratively, empirical evidence shows through distinguisher references [82] – [85] that in many burning cases in SRM the heating flux

rate fulfills $q_s \approx 5 \left[M \frac{W}{m^2} \right]$, using (26), the convective thermal coefficient is equal to $h_s = 1417.4 \left[\frac{W}{m^2 K} \right]$, where $T_s = 3550^0 C$, $T_i = 25^0 C$, respectively. Assuming [82] – [85] that in Carbon – Carbon heat protective insulation shield parameters are $T_{char} = 650^0 C$, $\rho_s = 2200 \left[\frac{kg}{m^3} \right]$, $C_p = 1350 \left[\frac{J}{kgK} \right]$, based on (27) – (28) the obtained values for the erosion rate and distance are $u_s = 0.58 [mm/\text{sec}]$ and $x_s = 3 [mm]$ for total burning time of 5.7sec, which are confirmed by the literature references [84] – [85] in the overloading erosion region. Suppose we have also radiation involved (from one surface to another only, $F_{1 \to 2} = 0.1$, $\sigma = 5.67 \cdot 10^{-8} [W/(m^2 K^4)]$), the contribution term to the erosion rate will be $0.14 [mm/\text{sec}]$ (see [86]) and the total theoretical value is about $u_{s, radiation\ and\ convection} = 0.72 [mm/\text{sec}]$.

5 2D thermo-elastic impact FEM simulation of elastic wave propagation inside protective composite made of homogenous isotropic material layers

As part of the examination of the shock wave's propagation along the composite material layers axial axis, a 2D finite elements simulation framework will be developed for four isotropic homogenous material's layers as follows: Steel - Al - Kevlar - Graphite.

The whole Abaqus FEM explicit transient temperature-displacement coupled equations are reported by Koric *et al.* [70], full procedure is brought there by Eqs. 1-24, while extensive numerical elasto-plastic method is brought by [71] - [72]. Based on Badurowicz and Pacekv [73], suppose we have both thermal energies accompanied with mechanical pressure, representing kinetic energy of a piercing bullet projectile into a given armor. While here, pre-heated projectile accompanied with mechanical pressure hitting frozen target is concerned. The Armor's axi-symmetrical geometry including the analysis properties, boundary and initial conditions (B. C., I. C.) appear in Table 1. Also, the armor materials properties layers are exhibited in Table 2. FEM axi-symmetrical analysis and modelling will be performed by Abaqus commercial software. For current instance, the land diameter of the contact area will be considered as the 5.56×45 [mm] NATO bullet [74]. The points of measurement for the principal stress were taken at the bottom base of each layer located in the axial axisymmetric axis, as shown in Fig. 1.

As expected, described in Fig. 5, SiCp material first layer absorbs high kinetic energy which yields meaningful thermal energy values that are conveyed / transformed to the next metallic steel layer, and so on, such as the mechanics loadings are absorbed by the metallic layers plates and the thermal loadings are absorbed by both metallic and non-metallic layers which increase the shield survivability and durability. Since the initial conditions occur under an extremely low temperature (-248.15$^0 C$), compressive stresses are developed, alternately, when the material experiences high temperature values, tensile stresses are developed. Since the heat is generated in short time through thermal shock, the compressive stresses are accompanied with tensile stresses and later through shock vibrations behavior, the compressive state is dominated over the tensile state.

The materials data is based on **MATWEB** database. One can infer from Fig. 5 that most metals (with the exception of the non - metallic Kevlar 49 and Crystalline Graphite) are able to experience high temperatures and high mechanical stresses, yet, as the metal is tending to be brittle together with mechanical strength increase, and hence its resistance to mechanical loads may increase, although simultaneously, its resistance to thermal loads may decrease.

6 FEM examination of particles effect on a 2D homogenous isotropic material layer subjected to thermo-elastic impact loading

Next step, a variety of insulation materials types, based on different shapes of pores filled with gas, fluid or solid (simulated as particles) states matter, will be tested separately for their resistance ability to withstand thermal shock using finite element commercial software 2D model. The FE model is based on heat transfer conduction mechanism for the following cases; (i) Different types of cavity filling (air, water, oil, Aluminum or metal); (ii) Different sizes of circular cross section filled cavities / particles; The current discussion is limited to orderly uniform particles partition and distribution along the material specimen as possible.

Jacob Nagler

The areas of interest that will be examined for adding particles and having the main absorption potential in the composite armor are the upper layer (1st) and the two lower layers (4th and 5th), so that most of the mechanical elastic wave part is absorbed by the upper layer, and from this, we would like to increase its properties for resistance to high thermal stresses while preserving its mechanical resistance against high mechanical impact elastic stresses, considering the weight of a minimal protective layer, optimally.

Moreover, we would like to improve the resistance of the ended two insulation layers of the shield to the development of elastic stresses during the optimization process of adding the particles, while subjected only to high temperature effect. It is important to define that these particles are part of the two-dimensional model and therefore the direction of length dimension into the page is infinite. Therefore, in reality, these particles will be considered as long cylindrical rods or as an array (row) of spherical / cylindrical particles, separated at a distance of up to about 5 millimeters from each other in such a manner that their continuity and mutual functioning and in relation to the protective layer will not be damaged.

The 2D thermal shock impact FEM simulation of elastic wave propagation (compression and tension are represented in the perpendicular principal stress plots by positive and negative signs, respectively) inside single protective homogenous isotropic material layer to be used as reference is depicted in Figs.6a – c. The numerical data values of elements type and number, boundary and initial conditions, geometry are elaborated in Table 3. We will mention that isotopic material has the same properties in *every direction* while homogenous material has the same properties at *every location* (point in the material). In our case, the particles are made of different materials and due to their size affects the non-homogeneity and non-isentropic nature of the whole layer that they reside in it. Figs. 7a-c illustrate the modelling and meshing of generalized layer with particles when configuration is altered according to the given data and configuration of material in Table 3. The point of measurements in all cases are in the bottom of the layer at the axi-symmetric axis as appear in Fig. 6c and Fig. 7c, respectively. Analyzing Fig. 8 might lead to the expectation / comprehension that Aluminum or Steel particles reduces

significantly the developed elastic wavy principal stresses over the different types of layers due to their thermo-mechanical ant thermal loadings, respectively. Specifically, for instance, Graphite layer without Al particles peak stress versus same single layer containing Al particles yields 50% decrease in peak stress; in the case of Steel particles it becomes 67% decrease difference. In the case of Kevlar 49, it is less significant than Graphite, Yet, comparison between Kevlar layers with Al or Steel particles relative to homogenous isotropic layers gives reduction percentage difference of 87.5% and 73.3%, respectively. In conclusion, Steel particles are most efficient to use as strengthen additive (positive material contamination) for the described homogenous layers. However, since the gain difference is not meaningful and since the ratio between the densities fulfills $\rho_{Al}/\rho_{Steel} \sim 1/3$, we would select the Aluminum particles to reduce the weight of the protective shield per layer.

Observing Fig. 9 for the various configurations of SiCp with and without various types of particles teaches that the existence of particles in the SiCp material increases significantly the chance to resist and withstand high thermo-mechanical loadings, particularly, Kevlar particles.

The Kevlar particles are not only support or provides elastic protection, which is already present in the ceramic material, but mainly provides thermal protection at a low weight compared to the metals, steel and aluminum and even the non-metallic Graphite. Particularly, for example, Graphite particles make the material less resistance against thermo-elastic shock even in relative to SiCp material with no particles at all (72% *increase* in impact peak stresses); The Kevlar 49 particles improves the resistance against impact peak stress by 22% (*reduction*) compared to Steel (35%) and Al (25%) which cause to peak stress *increase*, respectively.

Figs. 10a-b illustrations demonstrates that oil and water particles with coated elastic shell made of closed foam cells affects similarly (quantitatively and qualitatively) over the Graphite principal stress behavior thermal shock resistance performance. All kinds of fluid / gas shell particles making the Graphite layer less resistant against the thermal shock, while air particles have the highest weakening material potential. On the other hand, in the Kevlar 49 case, the air and oil particles behaves

/ affects similarly while this time, the water particles make it less resistant. In conclusion for both cases the gas and liquid particles makes both Kevlar 49 and Graphite materials less durable against the thermal shock (tens of percent decrease in resistance) which is confirmed qualitatively by the literature [63]. Alternatively, visco-elastic modelling should be considered in future instead of enclosed elastic foam.

7 FEM investigation of rigid particles effect on a 2D homogenous isotropic material layer subjected to thermo-elastic impact loading

Now, after selecting the most efficient and optimal weight layer – particles mixture, we will turn into particles size effect over the whole layer contained the suspended particles examination. Two kinds of layer examinations were performed:

- SiCp with immersed Kevlar 49 particles versus reference homogenous SiCp layer.
- Kevlar 49 layer containing Al particles versus reference homogenous Kevlar 49 layer.

The particles size diameters typical values of each examination were 0.3, 0.5 and $1mm$. The mesh and modelling appear in Fig. 11 and Table 4, respectively.

It is derived from Fig. 12a that in the case of Kevlar 49 lamina, the layer's resistance to thermal shock increases with increasing Al particle size. Although the quantitative difference between a particle of size $0.3mm$ and $0.5mm$ in the magnitude peak stress aspect is not significant (1% maximum and 0.5% maximum difference, respectively), yet, compared to 200% maximum difference in the case of $1mm$ diameter size. Accordingly, together with the consideration of the insulator weight $\rho_{Kevlar}/\rho_{Al}{\sim}0.54$, the particle diameter size of $0.5mm$ will be selected.

On the contrary, one can also infer from Fig. 12b that in the case of SiCp lamina, the layer's resistance to thermal shock decreases with increasing Kevlar 49 particle size. Although as similar to the previous case, the quantitative difference between a particle of size 0.3 and $0.5mm$ in the magnitude obtained peak stress aspect is not significant as in the case of $1mm$

diameter size (1% maximum compared to 176% maximum difference). Accordingly, together with the consideration of the insulator weight $\rho_{Kevlar}/\rho_{SiCp}{\sim}0.47$, the particle diameter size of $0.5\ mm$ will be selected.

8 FE final optimal axi-symmetrical composite layered model configuration results subjected to thermo-elastic impact loading

Finally, the selected layers mixed with the suspended selected particles material and size will be introduced compared with their counterparts without the internal particles through axi-symmetrical FE model. The mesh and modelling appear in Fig. 12 and Table 3, respectively.

Observing at Figs. 14a-b might lead to understanding that indeed the SiCp first layer with the Kevlar 49 particles experiences lower thermo-mechanical impact stress than the homogenous layer case without particles (25%). The Aluminum and Steel homogenous layers in both cases behave qualitatively and quantitatively the same. The Graphite 5th layer with the Al particles also exhibits lower peak principal stresses development than homogenous layer case in the initial composite configuration (400%). Nevertheless, the Kevlar 49 4th layer with particles presents less better performance (500%) due to the overall stress wave propagation through the materials layers, especially the 4th (Graphite) that transfers higher mechanical impact. Accordingly, we might re-select / alternate homogenous Kevlar 49 layer without particles instead the current Kevlar 49 layer with the Al particles. On the other hand, since the maximum principal stress value on the Kevlar 49 layer is about ~ 0.5GPa and the ultimate strength is about $\sim$3GPa, and therefore the existing layer could be utilized unchanged because the mechanical energy transferred to the 5th last protective layer is small enough.

Jacob Nagler

9 3D full ballistic impact FEM simulation of projectile propagation inside protective composite made of homogenous isotropic material layers and analysis

Suppose a projectile made of Tungsten [87, 88] gain velocity of $600 m/sec$ hitting a composite homogenous layered target initially pinned $(u_1 = u_2 = u_3 = 0)$ at 300K temperature based on the mechanical and damage properties given data in Table 2 and Table 5 during time of 0.006sec as appear in Fig. 15a. The obtained contact stress $(\sigma_{modified-HEL})$ in Eq. (3) will be $\sigma_{modified-HEL} = 10.5 [GPa]$. The approximate elastic modulus (21) required from the whole protective shield is equal to $E_{el} = \frac{\rho_p L_p L v^2}{x_{pl}^2} = \frac{15000 \cdot 55 \cdot 10^{-3} \cdot 14 \cdot 10^{-3} \cdot 600^2}{(2.3 \cdot 10^{-3})^2} \approx 800 [GPa]$. The dynamic friction between all shield plates was $\mu_{plates,d} = 0.5$ and combined tangential and normal behavior (Fig. 15b). The general dynamic friction value between the projectile body and shield plates was $\mu_d = 0.3$ and also assumed tangential and normal behavior (Fig. 15b). Each plate geometry was 100mmx100mmx2.8mm. The layers total thickness sum was 14mm. The projectile and each separate (individually) single protective layer nominal element size was 2mm and 2.5mm, respectively. Elements type in the whole analysis was C3D8R while projectile (partially) wedge elements type was C3D6 as appear in Fig. 16. The projectile finite elements model includes 1189 elements (1102 linear hexahedral elements of C3D8R type + 87 linear wedge elements of type C3D6) appropriate to 1500 nodes. Each finite element layer 1600 linear hexahedral elements of C3D8R type appropriate to 3362 nodes. The total assembly elements are summed to 9189 elements with 18310 nodes. The shield plates material order alongside the references, from up to bottom is: SiCp [87], Steel 304 [89], Al 7075-T651 [90], Kevlar 49 [91-93], Graphite Crystalline [94], respectively. Type of analysis performed using Abaqus commercial software was 3D stress dynamic linear explicit transient.

The selection of each material damage model was laid on their empirical behavior under axial impact as reported by [87] – [94] as appear in Table 5:

- The mechanism of tensile, compression and shear have been accounted for each material behavior.
- The Kevlar fiber plate was assumed to be isotropic and its properties were taken in the longitudinal projectile entrance direction only.

Analyzing the results appear in Figs. 17a-e show that the projectile stops by decreasing velocity and the shield configuration holding him and resist its full perforation (during the fourth Kevlar 49 layer penetration). It is also demonstrated by Von-Mises, Principal stress and displacement after 0.0006sec duration of time. Also, both analytically above calculations were confirmed by the results (be $\sigma_{modified-HEL} = 10.5 [GPa]$ versus $11[GPa]$ and the young's modulus calculation has proved to be effective prediction to the protective shield strength withstanding against the kinetic energy).

Note that the Graphite layer might be alternative replaced by the more lightweight material of aluminum foam, the results will be improved in the context of strength ballistic withstanding. The aluminum foam crushable model data can be found in [95] whereas the empirical material's nature appear in [96] – [97].

For each protective application it is always recommended to use the NATO standard STANAG (e.g. NATO STANAG 4569 for logistic and light armored vehicles, NATO STANAG 2920 for personal protective vest guard, etc.). In future, personal light weight protective configuration should be examined for seven layers (each single layer geometry is 100mmx100mmx3mm) against impact velocity higher than 600m/sec in the following order (1st configuration: AL/4BC – Boron Carbide - AL/4BC – Rubber - Boron Carbide – AL/4BC - Boron Carbide, 2nd configuration: SiCp - Boron Carbide – SiCp – Rubber – Dyneema - Boron Carbide - Dyneema, 3rd configuration: AL/4BC - Boron Carbide - AL/4BC – Rubber - AL/4BC - Boron Carbide - AL/4BC).

Jacob Nagler

10 Conclusion

Current study presented analytic development of modified Hugoniot elastic limit for composite double layer under thermal shock analytic model. Also, two-dimensional (2D) thermo-elastic impact FEM simulation response of elastic wave's propagation along the composite material layers axial axis made of homogenous isotropic material layers (Steel - Aluminum – Kevlar 49 - Graphite) was developed using commercial software (Abaqus) with explicit transient temperature-displacement coupled equations. The idea behind the mechanism was that SiCp material first layer absorbs high kinetic energy which yields meaningful thermal energy values that are conveyed / transformed to the next metallic steel layer, etc., such as the mechanics loadings are absorbed by the metallic layers plates and the thermal loadings are absorbed by both metallic and non-metallic layers which increase the shield survivability and durability. Accordingly, the layers improvement was focused on the upper layer (1st) and the two lower layers (4th and 5th), respectively, whilst most of mechanical elastic wave part is absorbed by the upper layer, and the thermal energy created could be absorbed by the two ended insulation layers. The idea is to improve the thermal energy resistance of the first insulation layer, and simultaneously, to increase the strength of the two ended insulation layers, while preserving the existing advantages qualities (properties) of each layer, without weakening them by the suspended particles.

Moreover, FEM examination of particles (oil, water, Aluminum or Steel) effect on a 2D homogenous isotropic material insulation layers subjected to thermo-elastic impact loading was performed in order to optimize the composite layered protective durability. Moreover, different sizes of selected materials' particles diameter were investigated in the context of developed principal peak stress during the thermo-elastic response. In all cases the principal stress was measured in the layer bottom at the axi-symmetrical axis. Also, in all cases a parentage difference comparison was made with the homogenous case. It was found that that Aluminum or Steel particles reduces significantly the developed elastic wavy

principal stresses over the different types of layers (i.e. Graphite or Kevlar layer containing Al or Steel particles) due to their thermo-mechanical ant thermal loadings, respectively. Although Steel particles are most efficient to use as strengthen additive for the described homogenous layers, yet, Aluminum particles were selected due to weight reduction per layer considerations. Additionally, the existence of particles in the SiCp material were found to increase significantly the chance to resist and withstand high thermo-mechanical loadings, particularly, Kevlar 49 particles compared to Steel and Al. All kinds of fluid / gas (water, oil and air) shell particles making the Graphite or Kevlar layers less resistant against the thermal shock, while air particles have the highest weakening material potential against thermal shock resistance performance as supported by literature [61].

Now, selecting the most efficient and optimal weight layer – particles mixture, we have investigated particles size effect over the whole layer contained the suspended particles examination; SiCp with immersed Kevlar 49 particles versus reference homogenous SiCp layer and Kevlar 49 layer containing Al particles versus reference homogenous Kevlar 49 layer. The particles size diameters typical values of each examination were 0.3, 0.5 and 1mm. It was derived that in Kevlar 49 lamina case, the layer's resistance to thermal shock increases with increasing particle size, in contrast, a vice versa behavior was found in the case of SiCp lamina. Although in both cases the quantitative difference between a particle of size 0.3mm and 0.5mm in the magnitude peak stress aspect was not found to be numerically significant, compared to 1mm diameter size. Accordingly, together with the consideration of the insulator weight the particle diameter size of 0.5mm was selected for both cases.

Finally, FE final optimal axi-symmetrical composite layered model subjected to thermo-elastic impact loading was analyzed. An overall good qualitative and quantitative resistant against thermo-mechanical impact was obtained by the composite armor with immersed particles compared to the composite layers without the particles. It was found that, indeed the SiCp first layer with the

Kevlar 49 particles, Graphite 5th layer with the Al particles experiences lower thermo-mechanical impact stress than the homogenous layer case without particles. The Aluminum and Steel homogenous layers in both cases behave qualitatively and quantitatively the same. The Graphite 5th layer with the Al particles also exhibits lower peak principal stresses development than homogenous layer case in the initial composite configuration. Although the Kevlar 49 4th layer with particles presents less better performance due to the overall stress wave propagation through the materials layers, especially the 4th (Graphite) that transfers higher mechanical impact. Accordingly, we might re-select / alternate homogenous Kevlar 49 layer without particles or alternatively, due to relatively small maximum principal stress value, the mechanical energy transferred to the 5th last protective layer is small enough, and hence to rely on the 4th layer as it is.

A dynamic Tungsten projectile full 3D case was examined over 5 layers target. The projectile was moving by velocity of 600m/sec hitting a composite homogenous layered target initially pinned ($u\_1=u\_2=u\_3=0$) at 300K temperature during penetration time of 0.006sec. The dynamic friction value between all shield plates was $\mu\_{(plates,d)}=0.5$ and combined tangential and normal behavior. Each plate geometry was 100mmx100mmx2.8mm. The layers total thickness sum was 14mm. The projectile and each separate (individually) single protective layer nominal element size was 2mm and 2.5mm, respectively. Type of analysis performed using Abaqus commercial software was 3D stress dynamic linear explicit transient analysis. The contact stress and the total elastic modulus were pre-calculated analytically and confirmed later through the analysis results. The shield plate's material order based on literature data from up to bottom was: SiCp - Steel 304 - Al 7075-T651 - Kevlar 49 - Graphite Crystalline, respectively.

The selection of each material damage model was laid on their empirical behavior under axial impact as reported by classical literature, considering the mechanism of tensile, compression and shear. The Kevlar fiber plate was assumed to be isotropic and its properties were taken in the longitudinal projectile entrance direction only. It was found that the projectile stopped by decreasing velocity and the shield configuration resistance from completing full perforation supported by projectile velocity alongside layers' stress and displacement results. In case the Graphite layer is alternatively replaced by the more lightweight material of aluminum foam, the results will be improved in the context of strength ballistic withstanding.

In future, further research should be made in the context of anisotropic and non-homogenous layers, especially on polymeric mixtures with and without particles, integrated or independent with metallic layers, subjected to thermo-mechanical impact loading during the short contact period. Also, visco-elastic modelling should be considered to model pores or particles filled with gas or fluid with instead of enclosed elastic foam.

Also, personal light weight protective configuration should be examined for seven layers (each single layer geometry is 100mmx100mmx3mm) against impact velocity higher than 600m/sec in the following order (1st configuration: AL/4BC – Boron Carbide - AL/4BC – Rubber - Boron Carbide – AL/4BC - Boron Carbide, 2nd configuration: SiCp - Boron Carbide – SiCp – Rubber – Dyneema - Boron Carbide - Dyneema, 3rd configuration: AL/4BC - Boron Carbide - AL/4BC – Rubber - AL/4BC - Boron Carbide - AL/4BC).

References

[1] Klett, J., Conway, B., 2000. Thermal management solutions utilizing high thermal conductivity graphite foams. In: Proceedings of the 45th International SAMPE Symposium and Exhibition, pp. 1933-1943.https://www.osti.gov/servlets/purl/770964

[2] Xie, Z., Wang, H., Deng, Q., Tian, Y., Shao, Y., Chen, R., Zhu, X., and Liao, Q., (2022) Heat transfer characteristics of Carbon-Based Photothermal Superhydrophobic materials with thermal insulation micropores during Anti-icing/Deicing, J. Phys. Chem. Lett. 13 (43), 10237–10244. DOI: 10.1021/acs.jpclett.2c02655

[3] Hu, Y., Mei, R., An, Z., Zhang, J., (2013) Silicon Rubber/ Hollow Glass Microsphere

composites: Influence of Broken Hollow Glass Microsphere on Mechanical and Thermal Insulation Property, Composites Science and Technology 79 64-69. DOI: 10.1016/j.compscitech.2013.02.015

[4] Azmi, W. H., Sharma, K. V., Mamat, R., Najafi, G., Mohamad, M.S. (2016) The enhancement of effective thermal conductivity and effective dynamic viscosity of nanofluids – A review, RSER 53 1046-1058. DOI: 10.1016/j.rser.2015.09.081

[5] Zhao, X. W., Zang, C. G., Sun, Y. L., Zhang, Y. L., Wen, Y. Q., Jiao, Q. J., (2018) Effect of hybrid hollow microspheres on thermal insulation performance and mechanical properties of silicone rubber composites, J. APPL. POLYM. SCI. 46025. DOI: 10.1002/app.46025

[6] Liu, X., Gui, N., Yang, X., Tu, J., and Jiang, S., (2021) A DEM-embedded finite element method for simulation of the transient heat conduction process in the pebble bed, Powder Technology. 377 607-620. DOI: 10.1016/j.powtec.2020.09.021

[7] Tomita, S., Celik, H., Mobedi, M. (2021) Thermal analysis of solid/liquid phase change in a cavity with one wall at periodic temperature. Energies 14, 5957. DOI: 10.3390/en14185957

[8] Zhang, C., Wang, Y., Jin, Z. G., Ke, H. B., and Wang, H., (2022) Experimental study of the thermal storage and mechanical properties of microencapsulated phase change composites during a supersonic cruise RSC Adv. 12, 6114-6121. DOI: 10.1039/D1RA08434H

[9] Kokabi, M., Bahramian, A. R., (2009) Ablation mechanism of polymer layered silicate nanocomposite heat shield, Journal of Hazardous Materials 166 445–454. DOI: 10.1016/j.jhazmat.2008.11.061

[10] Fesmire, J.E. (2016) Layered composite thermal insulation system for nonvacuum cryogenic applications, Cryogenics 74 154-165. DOI: 10.1016/j.cryogenics.2015.10.008

[11] Wang, Q., Han, X. H., Sommers, A., Park, Y., Joen, C.T., and Jacobi, A. (2012). A review on application of carbonaceous materials and carbon matrix composites for heat exchangers and heat sinks, IJR 35 7-26. DOI: 10.1016/j.ijrefrig.2011.09.001

[12] Gudivada, G., Kandasubramanian, B., (2019) Zirconium-Doped Hybrid Composite Systems for Ultrahigh Temperature Oxidation Applications: A Review, Ind. Eng. Chem. Res. 58, 4711−4731. DOI: 10.1021/acs.iecr.8b05586

[13] Xue, Y., Wang, H., Li, X., and Chen, Y., (2021) Exceptionally thermally conductive and electrical insulating multilaminar aligned silicone rubber flexible composites with highly oriented and dispersed filler network by mechanical shearing, Composites: Part A 144 106336. DOI: 10.1016/j.compositesa.2021.106336

[14] Zhang, X., Wang, Y., Wang, Y., Liu, B., and Bai, X., (2022) Preliminary study on the thermal insulation of a multilayer passive thermal protection system with carbon-phenolic composites in a combustion chamber, Case Studies in Thermal Engineering 35 102120. DOI: 10.1016/j.csite.2022.102120

[15] Renard, M., and Puszkarz, A.K., Modeling of Heat Transfer through Firefighters Multilayer Protective Clothing Using the Computational Fluid Dynamics Assisted by X-ray Microtomography and Thermography, Materials 15(15):5417. DOI: 10.3390/ma15155417

[16] Guo F, Zhao X, Tu W, Liu C, Li B, Ye J. Inverse Identification and Design of Thermal Parameters of Woven Composites through a Particle Swarm Optimization Method, Materials. 2023; 16(5):1953. DOI: 10.3390/ma16051953

[17] Zang, C., Pan, H., and Chen, Y. J., (2023) Synergistic Effects between Multiphase Thermal Insulation Functional Phases on the Mechanical and Heat Insulation Properties of Silicone Rubber Composites, ACS Omega 8 (31), 28026–28035. DOI: 10.1021/acsomega.2c03572

[18] Sha, W., Xiao, M., Zhang, J. et al. (2021) Robustly printable freeform thermal metamaterials, Nature Comm. 12 7228. DOI: 10.1038/s41467-021-27543-7

[19] Macak, J., Goniva, C., and Radl, S., (2023) Predictions of the P1 approximation for radiative heat transfer in heterogeneous granular media, Particuology 82 25-47. DOI: 10.1016/j.partic.2023.01.003

[20] Kılıç, N., Ekici, B., (2018) Ballistic resistance of high hardness armor steels against 7.62 mm armor piercing ammunition, Materials and Design, 44, 35–48. DOI: 10.1016/j.matdes.2012.07.045

[21] Hunter, S. C., (1957) Energy absorbed by elastic waves during impact, JMPS, 5, 162-171. DOI: 10.1016/0022-5096(57)90002-9

[22] Corcoran, J. C., and Kelly J. M., (1961) Phenomena of penetration in light weight rigid personnel armor materials, Beckman & Whitley, Dept. of Army Quartermasters Research and Engineering Command, AD273060. https://apps.dtic.mil/sti/pdfs/AD0273060.pdf

[23] Hutchings, I. M., (1979) Energy absorbed by elastic waves during plastic impact, J. Phys. D: Appl. Phys. 12 1819. DOI: 10.1088/0022-3727/12/11/010

[24] ARPA, (1964) Theoretical and experimental study of low-velocity penetration phenomena, Report, U. S. Army Natick Laboratories, Contract No. DA 19-129-AKC-150(X) (OI 9114). https://apps.dtic.mil/sti/pdfs/AD0467443.pdf

[25] Florence A. L., Ahrens, T. J., (1967) Interaction of projectiles and composite armor, Report, Stanford Research Institute Menlo Park, California 94025. https://apps.dtic.mil/sti/pdfs/AD0652726.pdf

[26] Asada, M. K., (1984) An analytical evaluation of spall suppression of impulsively loaded aluminum panels based on a one-dimensional stress wave propagation model, Thesis, Naval Postgraduate School, California. https://core.ac.uk/download/pdf/36712387.pdf

[27] Anderson, C. E. Jr., and Bodner, S. R., (1988) Ballistic impact: the status of analytical and numerical modeling, Int. J. Impact Eng. 7 (1), 9-35. DOI: 10.1016/0734-743X(88)90010-3

[28] Espinosa, H. D., Dwivedi, S., Zavattieri, P. D., and Yuan, G., (1998) A numerical investigation of penetration in multilayered material/structure systems, Int. J. Solid Struc. 35 (22), 2975-3001. DOI: 10.1016/S0020-7683(97)60353-4

[29] Herrmann, W., Bertholf, L.D., Thompson, S.L., (1975) Computational methods for stress wave propagation in nonlinear solid mechanics, In: Oden, J.T. (eds) Computational Mechanics. Lecture Notes in Mathematics, 461 Springer, Berlin, Heidelberg. DOI: 10.1007/BFb0074151

[30] Merzhievsky, L. A., Resnyansky, A. D. (1995) The role of numerical simulation in the study of high-velocity impact, International Journal of Impact Engineering, 17 4–6. DOI: 10.1016/0734-743X(95)99880-Z

[31] Corbett, G. G., Reid, S. R., and Johnson, W., (1996) Impact loading of plates and shells by free – flying projectiles: A review, International Journal of Impact Engineering, 18 141-230. DOI: 10.1016/0734-743X(95)00023-4

[32] Goldsmith, W., (1999) Review: Non-ideal projectile impact on targets, International Journal of Impact Engineering, 22 95—395. DOI: 10.1016/S0734-743X(98)00031-1

[33] Yarin, A. L., Roisman, I. V., Weber, K., Hohler, V., (2000) Model for ballistic fragmentation and behind-armor debris, International Journal of Impact Engineering, 24 171-201. DOI: 10.1016/S0734-743X(99)00048-2

[34] Nagler J. (2023) Thermoelastic impact modeling for projectile–target–muzzle components during penetration start of motion, The Journal of Defense Modeling and Simulation 0 1-23. DOI: 10.1177/15485129231210300

[35] Colen, A. J., Hanson, L. F., Frits G. R., and Hanson C. G. (2017) Thermal Energy Produced by Medium Velocity Pistol Projectiles and the Effects on Peripheral Nerve Tissue, SMRJ. 2 DOI:10.51894/001c.6345

[36] Kerampran, C., Tomasz, G., and Sielicki, P. W. (2020) Temperature Measurement of a Bullet in Flight, Sensors 20 7016. DOI: 10.3390/s20247016

[37] Wilkins, M. L., Cline, C. F., and Honodel C. A. (1969) Fourth Progress Report of Light Armor Program, Lawrence Radiation Laboratory, University of California, Livermore, UCRL - 50694. DOI: 10.2172/4173151

[38] Espinosa, H. D., Dwivedi, S., Zavattieri, P. D., and Yuan, G., (1998) A numerical investigation of penetration in multilayered material/structure systems, Int. J. Solid Struc. 35 (22), 2975-3001. DOI: 10.1016/S0020-7683(97)60353-4

[39] Kanel, G. I., Bless, S. J., and Rajendran, A. M. (2000) Behavior of brittle materials under dynamic loading, IAT. The University of Texas at Austin, IAT.R 0219. https://apps.dtic.mil/sti/pdfs/ADA386439.pdf

[40] Chandra, N., and Chen, X., (2003) Experimental characterization and modeling of damage in composites under ballistic impact, U.S. Army research office, ADA413347. https://apps.dtic.mil/sti/citations/tr/ADA413347

[41] Chen, X., Chandra, N., and Rajendran, A. M. (2004) Analytical solution to the plate impact problem of layered heterogeneous material systems, IJSS 41 4635 - 4659. https://doi.org/10.1016/j.ijsolstr.2004.02.064

Jacob Nagler

[42] Chen, X., Candara, N., and Rajendran, A. M. (2004) The effect of heterogeneity on plane wave propagation through layered composites, CST 64 1477 - 1493. DOI: 10.1016/j.compscitech.2003.10.024

[43] Colombo, P., Zordan, F., & Medvedovski, E. (2006). Ceramic–polymer composites for ballistic protection, Advances in Applied Ceramics 105 78–83. DOI: 10.1179/174367606X84440

[44] Rajendran, A.M., Ashmawi, W.M. and Zikry, M.A. (2006) The modeling of the shock response of powdered ceramic materials, Comput Mech 38 1–13. DOI: 10.1007/s00466-005-0712-3

[45] Gama, B. A., and Gillespie, J. W. Jr. (2011) Finite element modeling of impact, damage evolution and penetration of thick-section composites, IJIE 38 181-197. DOI: 10.1016/j.ijimpeng.2010.11.001

[46] Babaei, B., Shokrieh, M. M., and Daneshjou, K. (2011) The ballistic resistance of multi-layered targets impacted by rigid projectiles, 530 208-217. DOI: 10.1016/j.msea.2011.09.076

[47] Shanel, V., and Spaniel, M. (2014) Ballistic impact experiments and modelling of sandwich armor for numerical simulations, Procedia Engineering 79 230-237. DOI: 10.1016/j.proeng.2014.06.336

[48] Islam, R. I. Md. Zheng, J.Q., Batra, R. C. (2019) Ballistic performance of ceramic and ceramic-metal composite plates with JH1, JH2 and JHB Material Models, International Journal of Impact Engineering 137 103469. DOI: 10.1016/j.ijimpeng.2019.103469

[49] Peimaei, Y., and Khademian, N. (2020) Elasto-plastic simulation of bullet penetration into Al7075-SiCp composites armor, The 7th International Conference on Composites: Characterization, Fabrication and Application (CCFA-7), Tabriz, Iran. https://civilica.com/doc/1226067

[50] Fernando, P.L.N., Mohotti, D., Remennikov, A., Hazell, P. J., Wang, H., and Amin, A., (2020) Experimental, numerical and analytical study on the shock wave propagation through impedance-graded multi-metallic systems, IJMS 178 105621. DOI: 10.1016/j.ijmecsci.2020.105621

[51] Ranaweera, P., Weerasinghe, D., Fernando, P., Raman, S.N., and Mohotti, D. (2020) Ballistic performance of multi-metal systems, International Journal of Protective Structures 11 379-410. DOI: 10.1177/2041419619898693

[52] Goda, I., and Girardot, J. (2021) Numerical modeling and analysis of the ballistic impact response of ceramic/composite targets and the influence of cohesive material parameters, International Journal of Damage Mechanics 30 1079-1122. DOI:10.1177/1056789521992107

[53] Jasra, Y., and Saxena, R. K. (2022) Fracture behavior of prestressed ductile target subjected to high velocity impact – Numerical study, ACM 16 101-118. https://acm.kme.zcu.cz/acm/article/view/779

[54] Gautam, P. C., Gupta, R. Sharma, A. C., and Singh, M. (2017) Determination of Hugoniot Elastic Limit (HEL) and Equation of State (EOS) of Ceramic Materials in the Pressure Region 20 GPa to 100 GPa, Procedia Engineering 173 198 – 205. DOI: 10.1016/j.proeng.2016.12.058

[55] Sauer, C., Bagusat, F., Ruiz-Ripoll, M. L., Roller, C., Sauer, M., Heine, A., and Riedel, W. (2022) Hugoniot data and equation of state parameters for an ultra-high-performance concrete, J. dynamic behavior mater. 8, 2–19. DOI: 10.1007/s40870-021-00315-6

[56] Kanel, G. I., Razorenov, S. V., Utkin, A. V., Fortov, V. E., Baumung, K., Karow, H. U., Rusch, D., and Licht, V. (1993) Spall strength of molybdenum single crystals, J. Appl. Phys. 74 7162–7165. DOI: 10.1063/1.355032

[57] Joshi, K. D., Rav, A. S., Gupta, S. C., and Banerjee, S., (2010) Measurement of spall strength of A12024-T4 and SS304 in plate impact experiments, J. Phys.: Conf. Ser. 215 012149. DOI: 10.1088/1742-596/215/1/012149

[58] Mukherjee, D., Rav, A., Sur, A., Joshi, K. D., and Gupta, S. C. (2014) Shock induced spall fracture in polycrystalline copper, AIP Conf. Proc. 24 1591 608–610. DOI: 10.1063/1.4872691

[59] Shawoon K. R., Trabia, M., O'Toole, B., Hixson, R., Becker, S., Pena, M., Jennings, R., Somasoundaram, D., Matthes, M., Daykin, E., Machorro, E. (2016) Study of Hypervelocity Projectile Impact on Thick Metal Plates, Shock and Vibration 2016, Article ID 4313480, 1-11. DOI: 10.1155/2016/4313480

[60] Li, D., Li, W., Li, D., Shi, Y., and Fang, D. (2013) Theoretical research on thermal shock resistance of ultra-high temperature ceramics focusing on the adjustment of stress reduction factor, Materials 6 551-564. DOI: 10.3390/ma6020551

[61] Wang, R. and Li, W. (2017) Characterization models for thermal shock resistance and fracture strength of ultra-high temperature ceramics at high temperatures, Theoretical and Applied Fracture Mechanics 90 1-13. DOI: 10.1016/j.tafmec.2017.02.005

[62] Kou, W., Li, W., Cheng, T., Li, D., and Wang, R. (2017) Thermal shock resistance of ultra-high temperature ceramics under active cooling condition including the effects of external constraints, ATE 110 1247-1254. DOI: 10.1016/j.applthermaleng.2016.09.004

[63] Wei, W., Song, Y., Yang, Z., Gao, G., Xu, P., Lu, M., Tu, C., Chen, M., and Wu, G. (2019) Investigation of the impacts of thermal shock on carbon composite materials, Materials 12, 435. DOI: 10.3390/ma12030435

[64] Ramírez-Gil, F. J., Silva, E. C. S., Montealegre-Rubio, W. (2021) Through-thickness perforated steel plates optimized for ballistic impact applications, Materials & Design 212 110257. DOI: 10.1021/acs.iecr.8b05586

[65] Li, L., Zhang, Q. C., and Lu, T. J. (2022) Ballistic penetration of deforming metallic plates: Experimental and numerical investigation, IJIE 170 104359. DOI: 10.1016/j.ijimpeng.2022.104359

[66] Wen, Z., Tang, Z., Liu, Y., Zhuang, L., Yu, H., and Chu, Y. (2024) Ultrastrong and High Thermal Insulating Porous High-Entropy Ceramics up to 2000 °C. Adv. Mater, 36, 2311870. DOI: 10.1002/adma.202311870

[67] Christiansen, E. L. (1991) Shield Sizing and Response Equations, NASA, Lyndon B. Johnson Space Center Houston, Texas 77058. https://ntrs.nasa.gov/citations/19920010785

[68] Natali, M., Kenny, J. M., and Torre, L. (2016) Science and technology of polymeric ablative materials for thermal protection systems and propulsion devices: A review, PMS 84 192-275. DOI: 10.1016/j.pmatsci.2016.08.003

[69] Oved, Y., Luttwak, G. E., and Rosenberg, Z., (1978) Shock wave propagation in layered composites, JCM 12 84-96. DOI:10.1177/002199837801200107

[70] Koric, S., Hibbeler, L.C., and Thomas B.G. (2009) Explicit coupled thermo-mechanical finite element model of steel solidification, Int. J. Numer. Meth. Engng. 78 1-9. DOI: 10.1002/nme.2476

[71] Ming, L. and Pantalé, O. (2018) An efficient and robust VUMAT implementation of elastoplastic constitutive laws in Abaqus/Explicit finite element code, Mechanics & Industry 2018; 19: 308. DOI: 10.1051/meca/2018021

[72] Abaqus Software Manual, (2022): https://docs.software.vt.edu/abaqusv2022/Engl ish/SIMACAEANLRefMap/simaanl-c-couptempdisp.htm

[73] Badurowicz P and Pacek D. (2022) Determining ricocheting projectiles' temperature using numerical and experimental approaches, Materials 2022 15 928. DOI: 10.3390/ma15030928

[74] Kolmakov, A.G., Bannykh, I.O., Antipov, V.I., Vinogradov, L.V., and Sevost'yanov, M.A. (2021) Materials for bullet cores, Russ. Metall 2021: 351–362. DOI:10.1134/S0036029521040133

[75] Nagler, J. (2021) On analytical ballistic penetration fundamental model and design, WSEAS TRANSACTIONS on HEAT and MASS TRANSFER, 16 177-191. DOI: 10.37394/232012.2021.16.21

[76] Nagler, J. (2022) Simple approximate solutions for dynamic response of suspension system, WSEAS TRANSACTIONS on SYSTEMS, 21 20-31. DOI: 10.37394/23202.2022.21.2

[77] Dieter G. E. (1986) Mechanical behavior under tensile and compressive loads, ASM Handbook 8 99–10. DOI: 10.31399/asm.hb.v08.a0003261

[78] Liu, B., Villavicencio, R., and Soares, C. G. (2013) Failure characteristics of strength-equivalent aluminium and steel plates in impact conditions in: Analysis and Design of Marine Structures – Guedes Soares & Romanoff (eds), Taylor & Francis Group, London, ISBN 978-1-138-00045-2, 167-174. DOI: 10.1201/b15120-25

[79] Seisson, G., Hebert, D., Bertron, I., Chevalier, J. M., Hallo, L., Lescoute, E., Videau, L., Combis, P., Guillet, F., Boustie, M., and Berthe, L. (2013) Dynamic cratering of graphite: experimental results and simulations, International Journal of Impact Engineering 63 18- 28. DOI: 10.1016/j.ijimpeng.2013.08.001

[80] Manigandan, S. (2015) Computational investigation of high velocity ballistic impact test on Kevlar 149, AMM 766-767 1133-1138. DOI: 10.4028/www.scientific.net/AMM.766-767.1133

[81] Li, G. (2017) Impact modelling of Kevlar fabric composite panels, Conference: 63rd CASI Aeronautics Conference and 24th CASI Aerospace Structures & Materials Symposium

At: Toronto. https://www.researchgate.net/publication/3207 36489_Impact_Modelling_of_Kevlar_Fabric_ Composite_Panels

[82] Sun, L., Bao, F., Zhang, N., Hui, W., Wang, S., Zhang, N., and Deng, H. (2016) Thermo-structural response caused by structure gap and gap design for solid rocket motor nozzles, Energies 9 430. DOI: 10.3390/en9060430

[83] Concio, P., Migliorino, M.T. and Nasuti, F. (2021) Numerical approach for the estimation of throat heat hlux in liquid rocket engines. Aerotec. Missili Spaz. 100 33–38. DOI: 10.1007/s42496-020-00060-4

[84] Wang, L., Tian, W., Chen, L. et al. (2021) Investigation of Carbon–Carbon nozzle throat erosion in a solid rocket motor under acceleration conditions. Int. J. Aeronaut. Space Sci. 22 42–51. DOI: 10.1007/s42405-020-00277-4

[85] Tian, H., He, L., Yu, R., Zhao, S., et al. (2021) Transient investigation of nozzle erosion in a long-time working hybrid rocket motor, AST 118 106978. DOI: 10.1016/j.ast.2021.106978

[86] Turchi, A., Bianchi, D., Thakre, P., Nasuti, F., and Yang, V. (2014) Radiation and roughness effects on nozzle thermochemical erosion in solid rocket motors, Journal of Propulsion and Power 30, 314-324. DOI: 10.2514/1.B34997

[87] Sun, M., Cao, W., Hu, D., Zhang, N., and Chi, R. (2021) Effect of Cover Plate on the Ballistic Performance of Ceramic Armor. Materials 14 1. DOI: 10.3390/ma14010001

[88] Holmquist, T. J., Johnson, G. R., and Gooch, W. A. (2005) Modeling the 14.5 mm BS41 projectile for ballistic impact computations (originally from the book: Computational Ballistics II), WIT Transactions on Modelling and Simulation 40 61-75.https://www.witpress.com/Secure/elibrary/p apers/CBAL05/CBAL05007FU.pdf

[89] Dean, J., Fallah, A. S., Brown, P. M., Louca, L. A. and Clyne, T. W. (2011) Energy absorption during projectile perforation of lightweight sandwich panels with metallic fibre cores, Composite Structures 93 1089-1095. DOI:10.1016/j.compstruct.2010.09.019

[90] Aslam, M. A., Ke, Z., Rayhan, S. B., Faizan, M., and Bello, I. M. (2020) An investigation of soft impacts on selected aerospace grade alloys based on Johnson-Cook material model, J. Phys.: Conf. Ser. 1707

012008.DOI: 10.1088/1742-6596/1707/1/012008

[91] Zhu, D., Mobasher, B., Rajan, S.D. (2011) Dynamic tensile testing of Kevlar 49 fabrics, J Materials in Civil Eng, 23 1-10.DOI:10.1061/(ASCE)MT.1943-5533.0000156

[92] Zhu, D., Vaidya, A., Mobasher, B., and Rajan, S. D. (2014) Finite element modeling of ballistic impact on multi-layer Kevlar 49 fabrics, Composites: Part B 56 254–262. DOI: 10.1016/j.compositesb.2013.08.051

[93] Xuan, H., Hu, Y., Wu, Y. and He, Z. (2018) Containment ability of Kevlar 49 composite case under spinning impact, J. Aerosp. Eng., 31 04017096.DOI: 10.1061/(ASCE)AS.1943-5525.0000806

[94] Seisson, G., Hebert, D., Bertron, I., Chevalier, J. M., Hallo, L., et al. (2013) Dynamic cratering of graphite: experimental results and simulations, International Journal of Impact Engineering, 63, 18-28.DOI: 10.1016/j.ijimpeng.2013.08.001

[95] Novak, N., Vesenjak, M., Duarte, I., Tanaka, S., Hokamoto, K., Krstulović-Opara, L., Guo, B., Chen, P., and Ren, Z. (2019) Compressive Behaviour of Closed-Cell Aluminium Foam at Different Strain Rates. Materials 12, 4108. DOI: 10.3390/ma12244108

[96] Vengatachalama, B., Poh, L. H., Liu, Z. S., Qinc, Q. H., Swaddiwudhipong, S. (2019) Three-dimensional modelling of closed-cell aluminium foams with predictive macroscopic behavior, Mechanics of Materials, 136 103067.DOI: 10.1016/j.mechmat.2019.103067

[97] Chi, R., Serjouei, A., Sridhar, I., and Tan, G.E.B. (2013) Ballistic impact on bi-layer alumina/aluminium armor: A semi-analytical approach, IJIE 52 37-46. DOI: 10.1016/j.ijimpeng.2012.10.001

[98] Moslemi Petrudi, A., Vahedi, K., Rahmani, M., and Moslemi Petrudi, M. (2020) Numerical and analytical simulation of ballistic projectile penetration due to high velocity impact on ceramic target. Frattura Ed Integrità Strutturale 14 226–248.DOI: 10.3221/IGF-ESIS.54.17

[99] Sundaram, S. K., Bharath A. G., and Aravind B. (2020) Influence of target dynamics and number of impacts on ballistic performance of 6061-T6 and 7075-T6 Aluminum alloy targets, Mechanics Based Design of Structures and Machines 50 993–1011.DOI:10.1080/15397734.2020.1738245

[100] Pacek, D. and Badurowicz, P. (2024) Numerical and experimental analysis of the

influence of projectile impact angle on armour plate protection capability, Defence Science Journal, 74 439-446. DOI: 10.14429/dsj.74.19308

[101] Goda, I. (2023) Ballistic resistance and energy dissipation of woven-fabric composite targets: insights on the effects of projectile shape and obliquity angle, Defence Technology, 14-32.DOI: 10.1016/j.dt.2022.06.008

[102] Rodríguez-Millán, M., Díaz-Álvarez, A., Bernier, R., Miguélez, M. H., Loya, J. A. (2019) Experimental and numerical analysis of conical projectile impact on Inconel 718 Plates, Metals 9, 638. DOI: 10.3390/met9060638

[103] Reyssat, E., Tallinen, T., Le Merrer, M., Mahadevan, L. (2012) Slicing softly with shear, Phys. Rev. Lett. 109, 244301. DOI: 10.1103/PhysRevLett.109.244301

[104] Deibel K.R., Lammlein, S., and Wegener, K. (2014) Model of slice-push cutting forces of stacked thin material, JMPT 214 667-672. DOI: 10.1016/j.jmatprotec.2013.10.009

[105] Mora, S., Tallinen, and Pomeau, Y. (2020) Cutting and slicing weak solids, Phys. Rev. Lett. 125, 038002. DOI:10.1103/PhysRevLett.125.038002

[106] Mora, S. (2021) Effects of the blade shape on the slicing of soft gels. Eur. Phys. J. E 44, 151. DOI: 10.1140/epje/s10189-021-00158-y

[107] Arnbjerg-Nielsen, S. F., Biviano, M. D. and Jensen, K. H. (2024) Competition between slicing and buckling underlies the erratic nature of paper cuts, Phys. Rev. E 110 025003. DOI: 10.1103/PhysRevE.110.025003

Contribution of Individual Authors to the Creation of a Scientific Article (Ghostwriting Policy)

The author contributed in the present research, at all stages from the formulation of the problem to the final findings and solution.

Conflict of Interest

The author has no conflict of interest to declare that is relevant to the content of this article.

APPENDIX
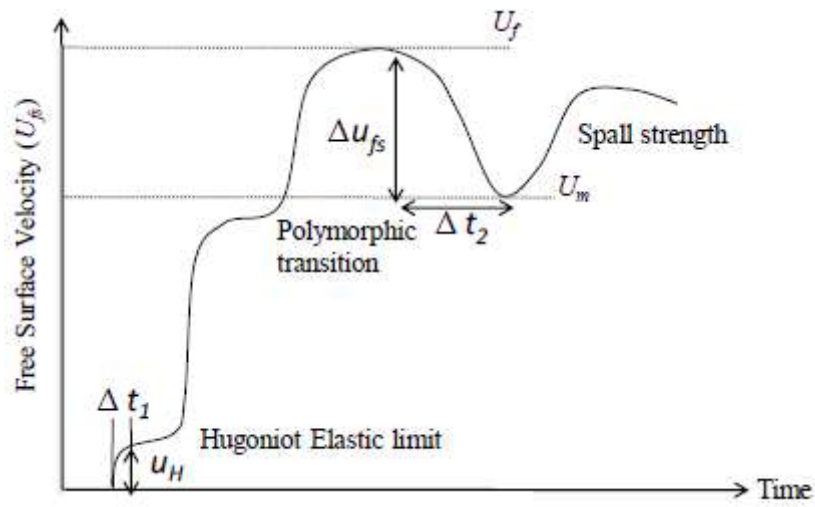
Fig. 1 Ideal free surface velocity profile versus time to exemplify the Hugoniot elastic limit and the spall strength

Jacob Nagler
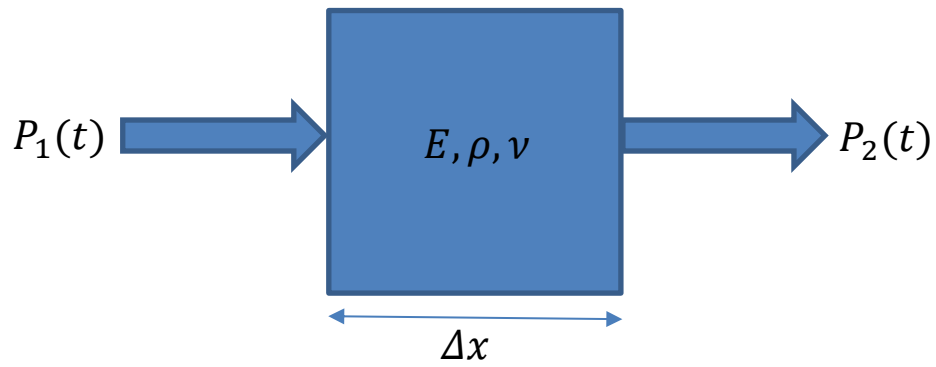
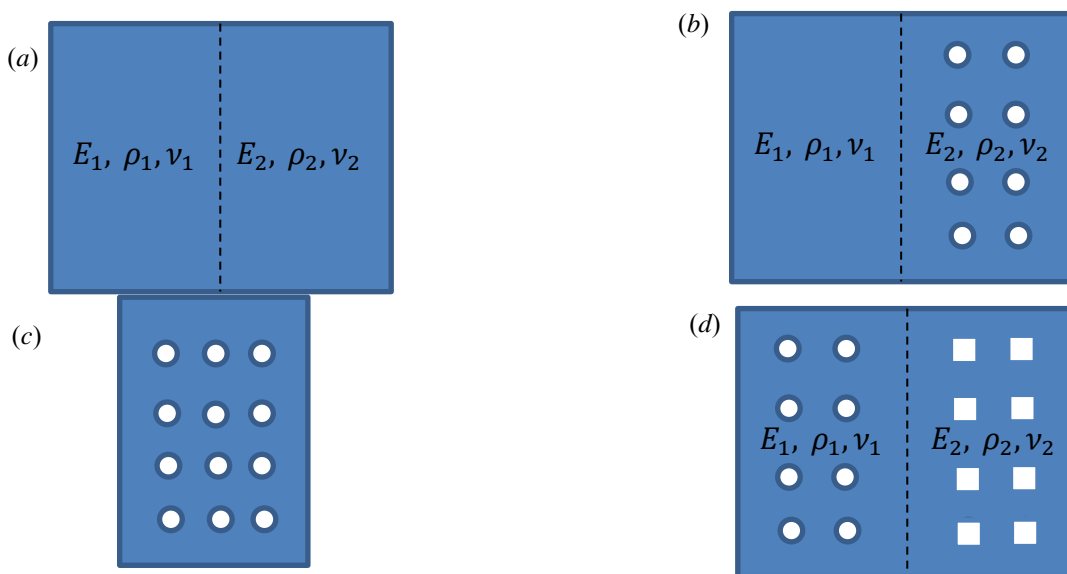Fig. 2 (*a*) material specimen subjected to general thermo-elastic impact loading

Fig. 3 Two-dimensional generalized double layer protection shield material schematic description: (*a*) Two adjacent different materials protective shield (*b*) Two adjacent different materials protective shield with one side pores or particles (*c*) Homogenous protective shield material with pores or particles (*d*) Two adjacent different materials protective shield consisting different pores or particles
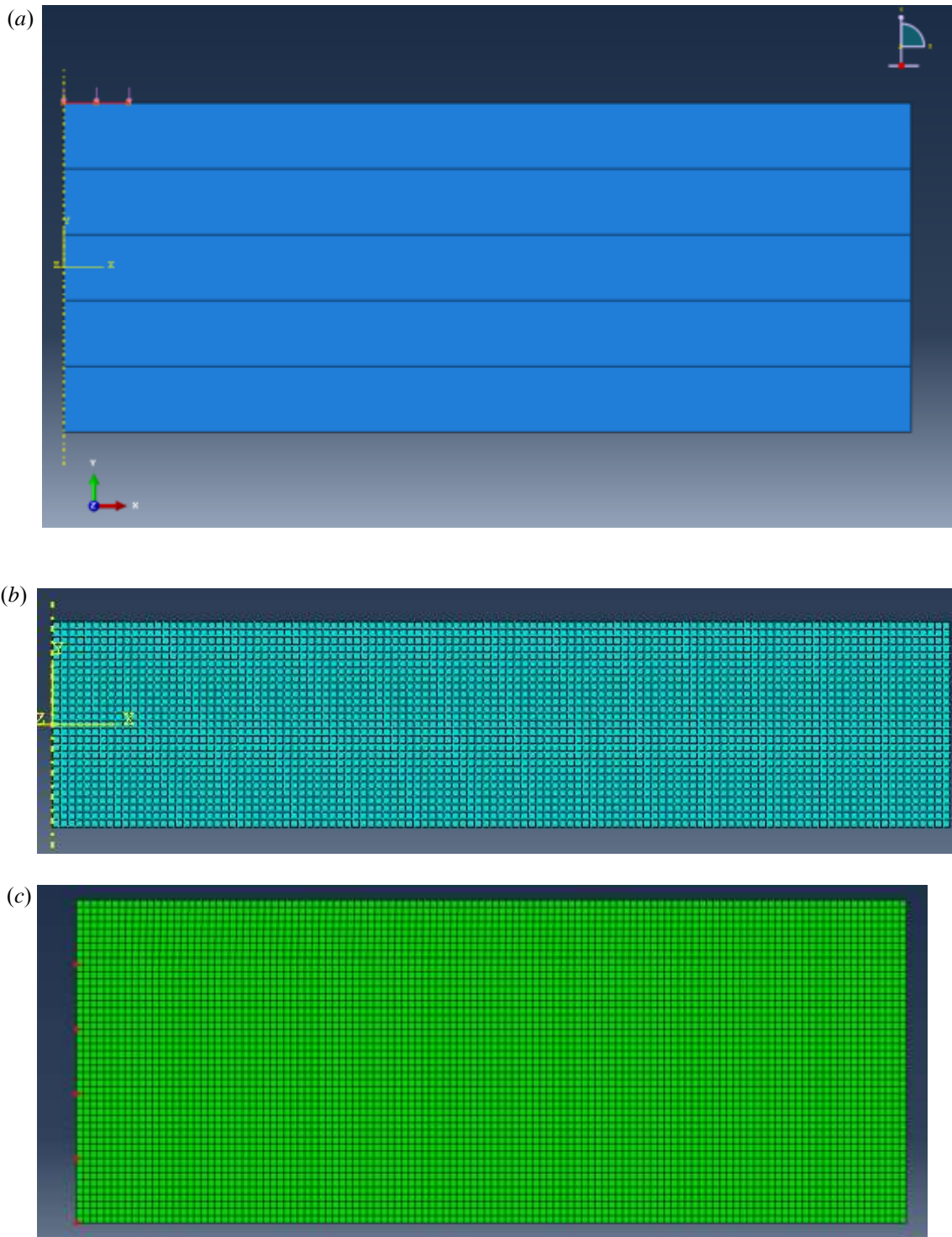
Fig. 4 Circular plate axi-symmetrical FE model: (*a*) Boundary conditions (*b*) FEM meshing model. (*c*) Points of measurements (Marked by Red points)
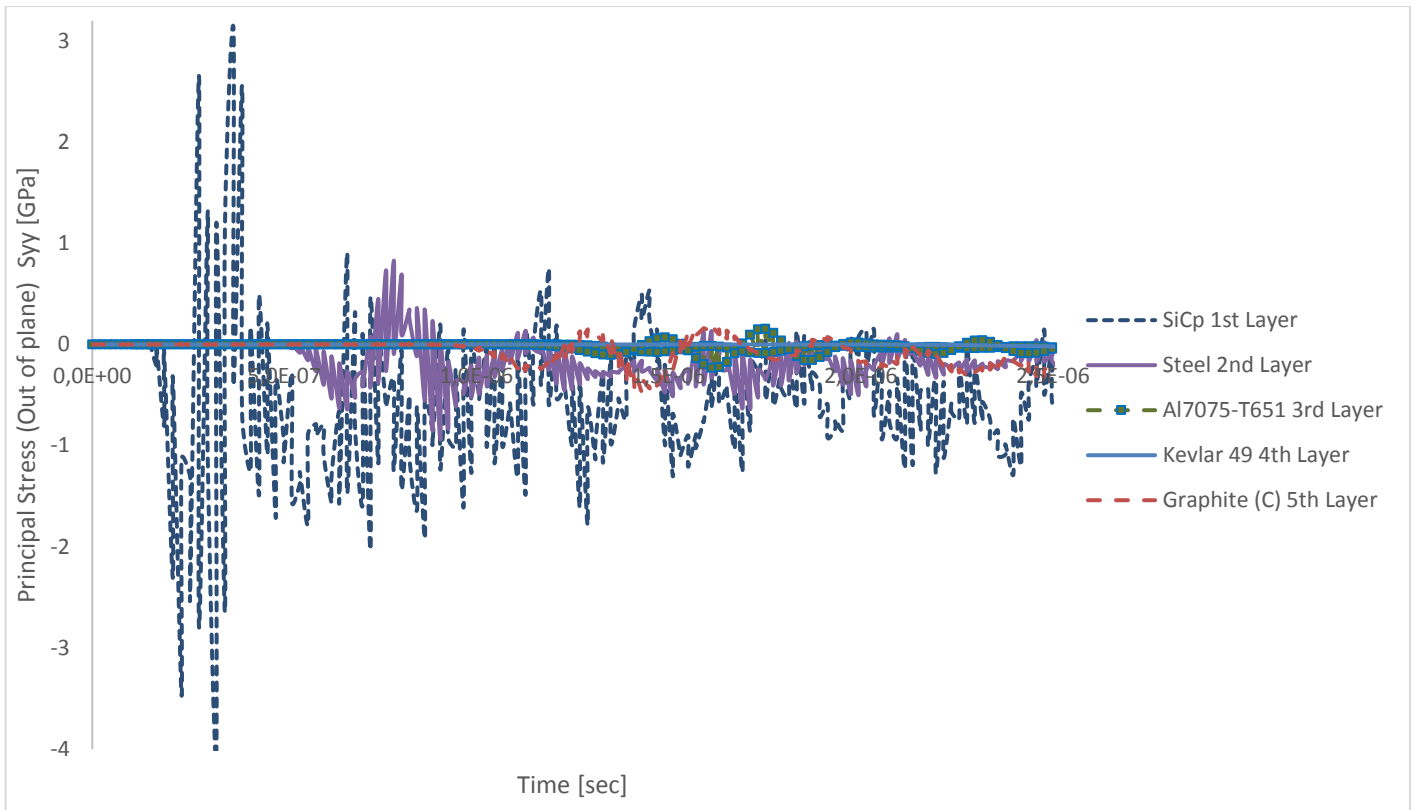
Fig. 5 Composite metallic circular plate axi-symmetrical FE 2D model results

(a)

(b)

(*c*)
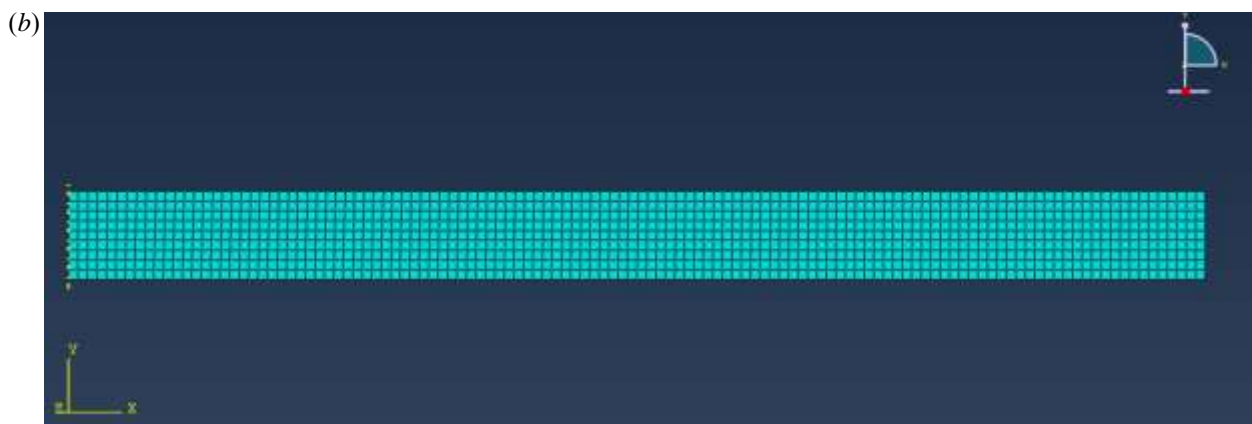
Fig. 6 Circular homogenous isotropic plate axi-symmetrical FE model: (*a*) Boundary conditions (*b*) FEM meshing model. (*c*) Points of measurements (Marked by Red points)

(*a*)

(*b*)

(*c*)
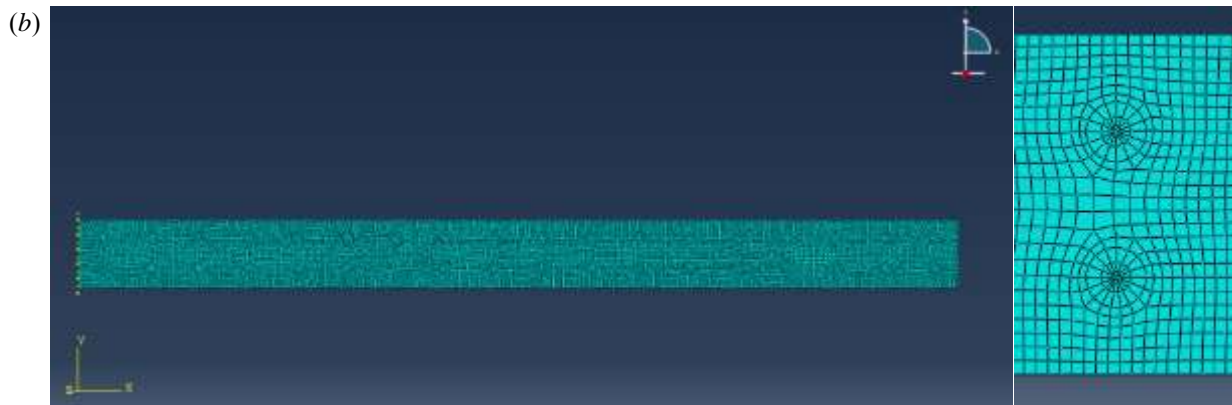
Fig. 7 Circular plate axi-symmetrical FE model with particles: (*a*) Boundary conditions (*b*) FEM meshing model. (*c*) Points of measurements (Marked by Red points)
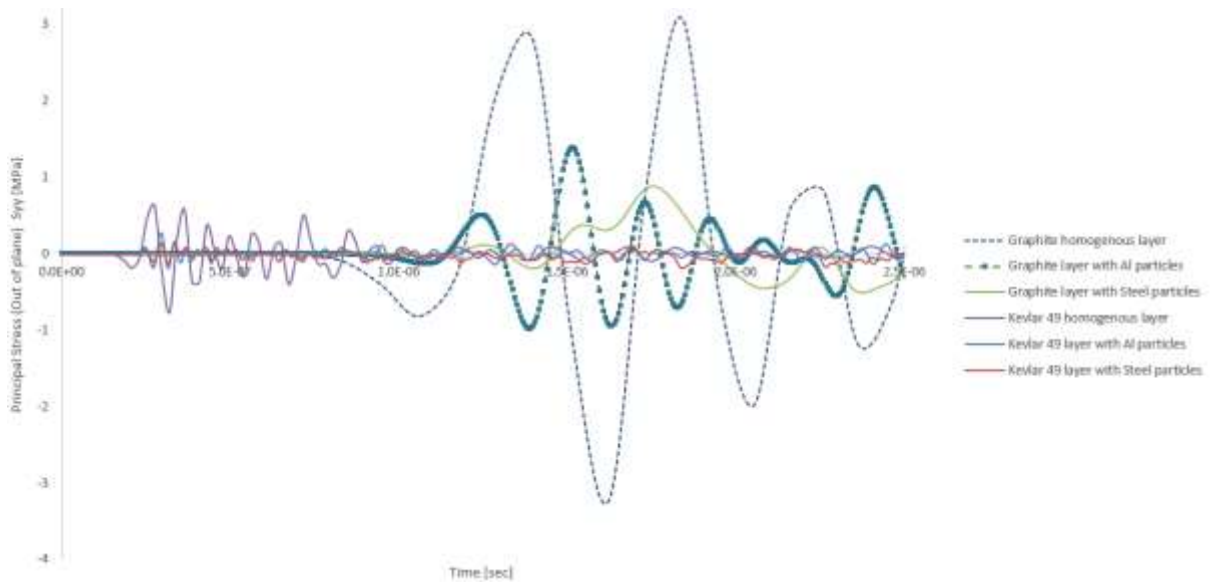
Fig. 8 Graphite versus Kevlar materials single layer under thermal shock 2D FEM model results
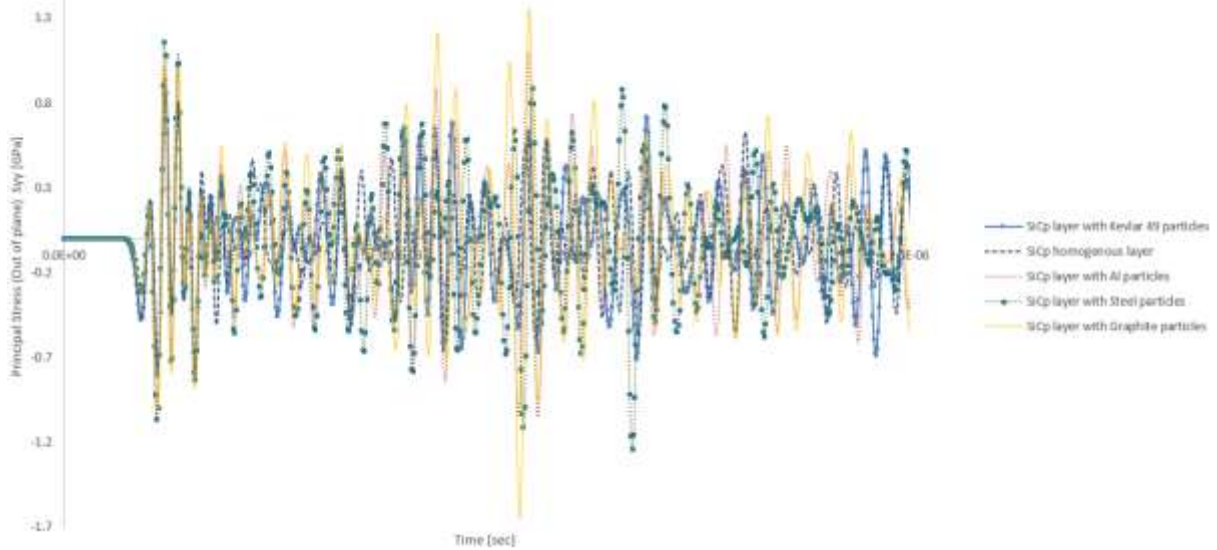
Fig. 9 SiCp versus Steel materials single layer (Al, steel. SiCp) under thermo-elastic shock 2D FEM model results

(*a*)

(*b*)
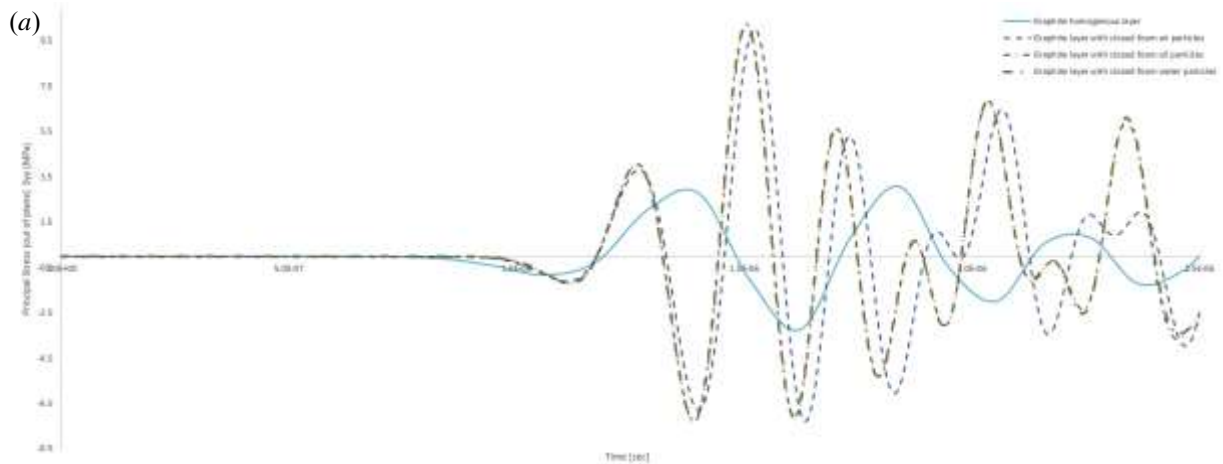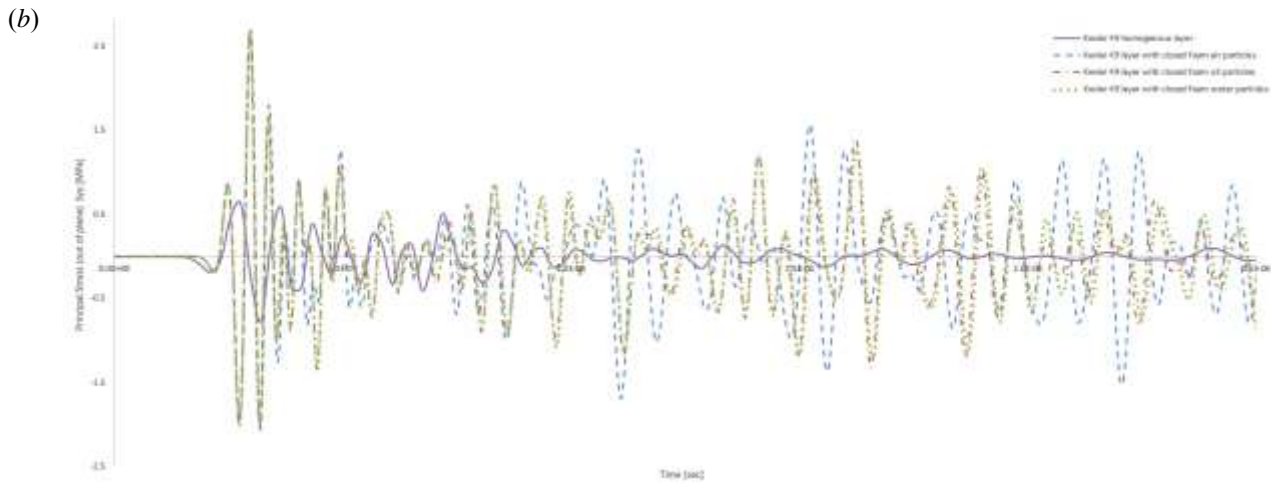
Fig. 10 (*a*) Graphite versus (*b*) Kevlar materials (air, oil, water) single layer under thermal shock 2D FEM heat - transfer model results
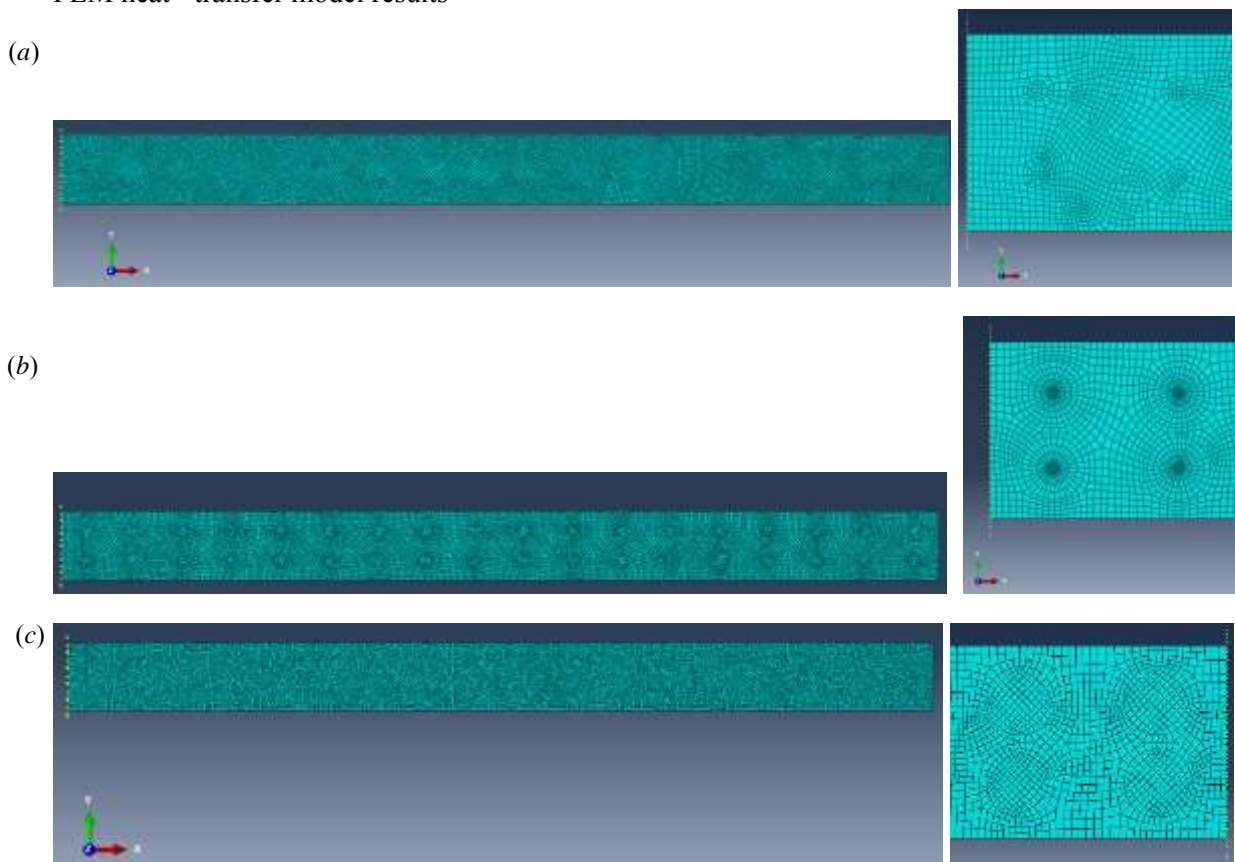
(*a*)

(*b*)

(*c*)

Fig. 11 Circular plate axi-symmetrical FE meshing model with different particles sizes: (*a*) 0.3*mm* (*b*) 0.5*mm* (*c*) 1*mm*
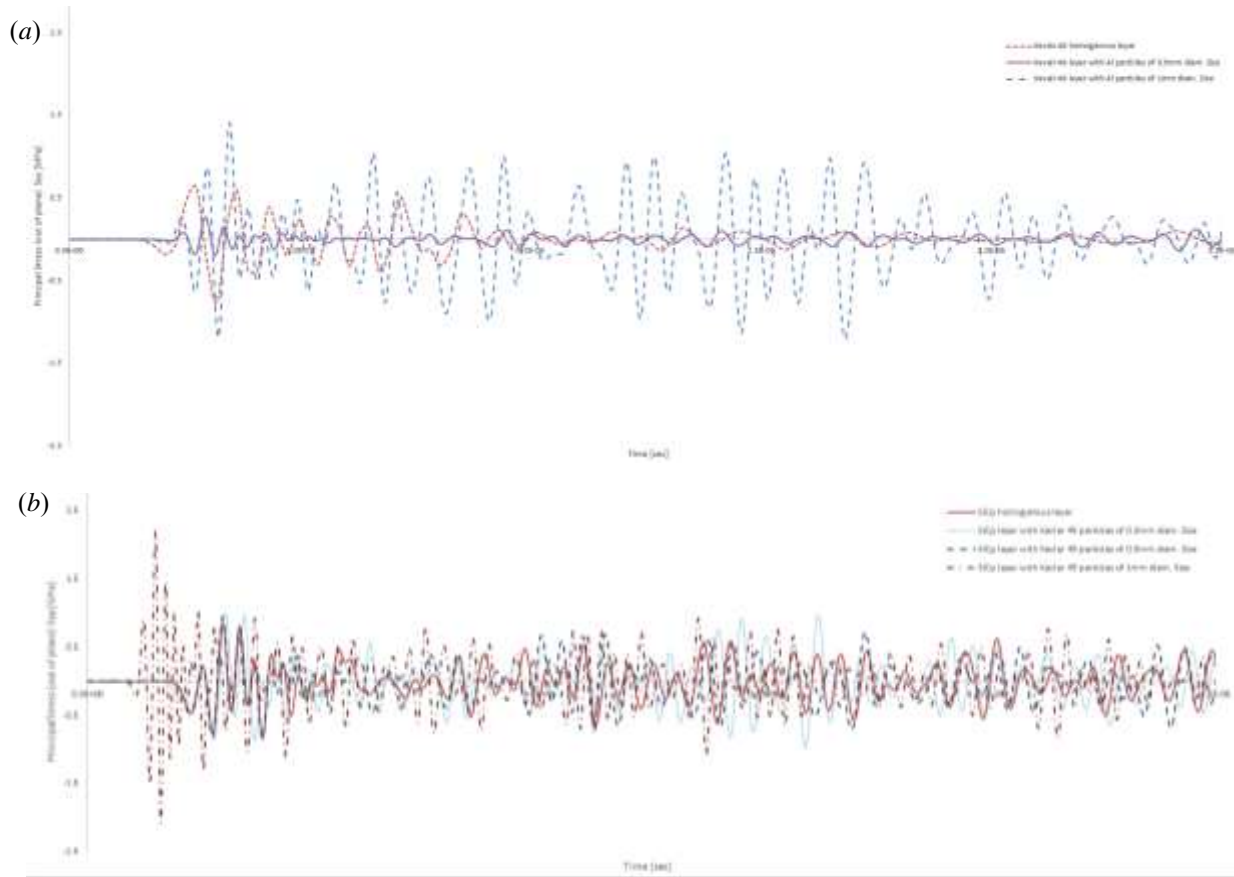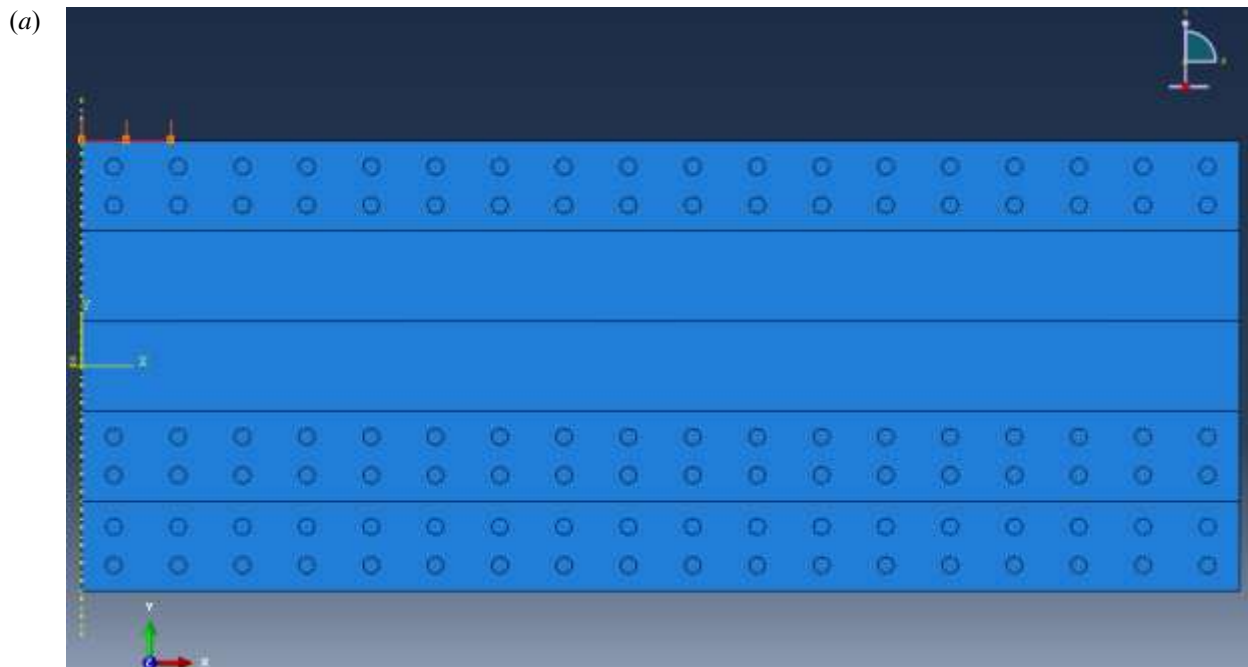
(*a*)

(*b*)

Fig. 12 plots of selected configuration under the influence of various particles size effects
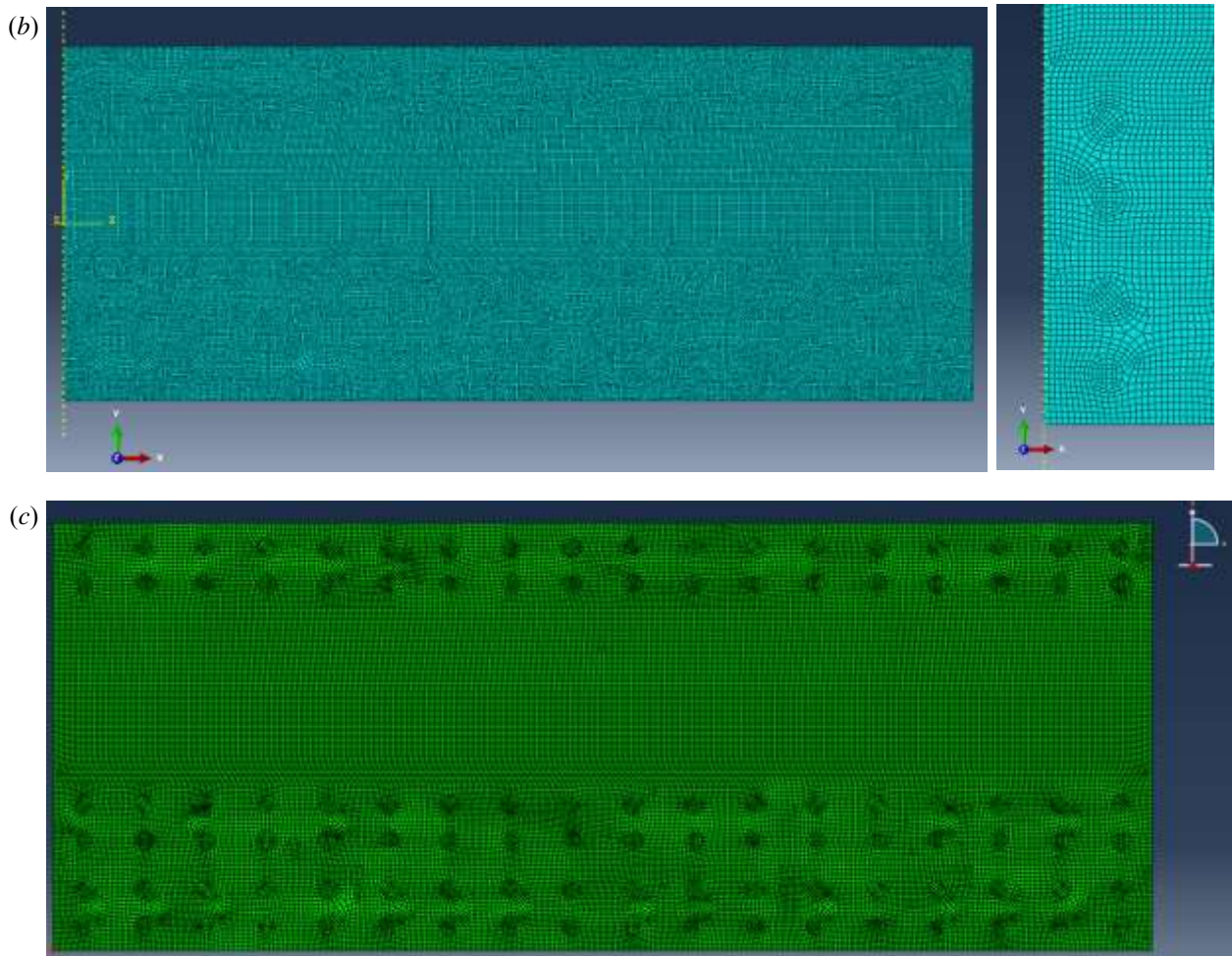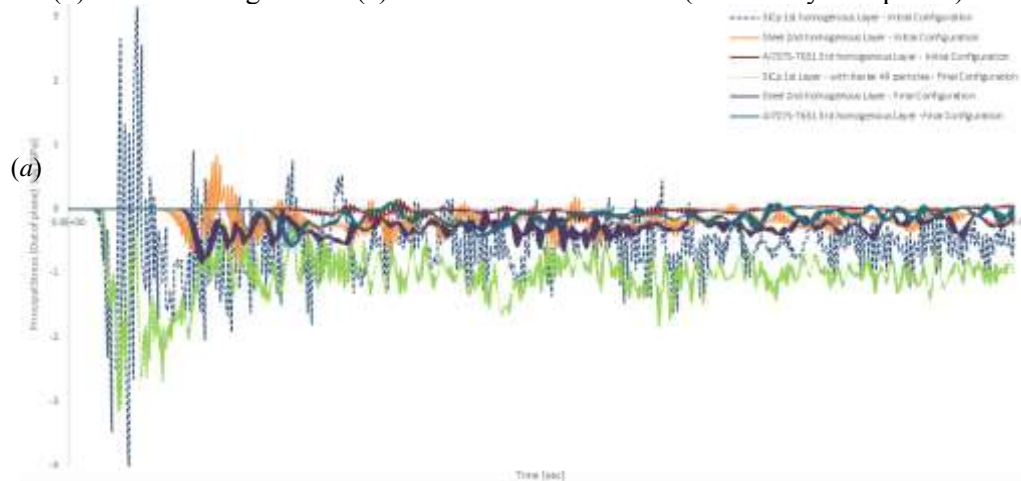
(*a*)

(*b*)

(*c*)

Fig. 13   Circular plate axi-symmetrical FE optimized composite model configuration: (*a*) Boundary conditions (*b*) FEM meshing model. (*c*) Points of measurements (Marked by Red points)
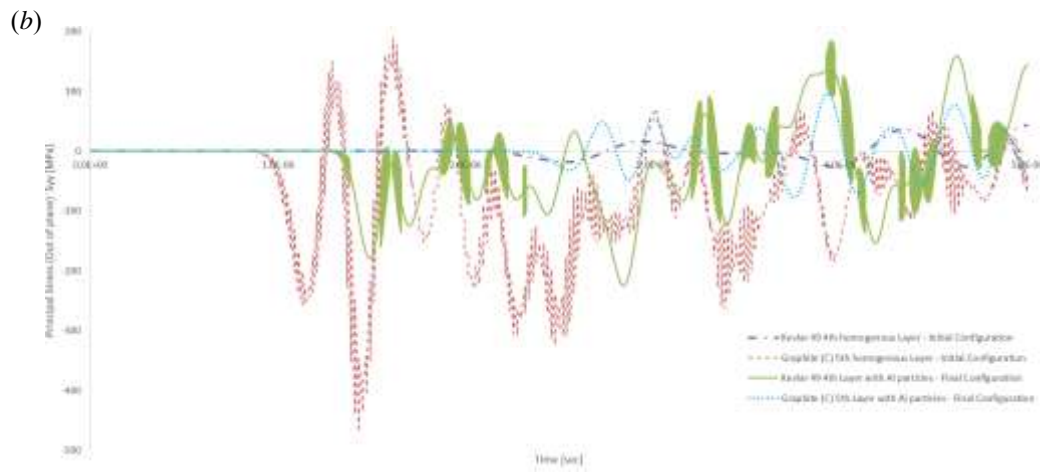
(*a*)

Fig. 14 Upgraded composite metallic circular plate axi-symmetrical FE 2D model results with particles versus the initial composite configuration made of homogenous layers.
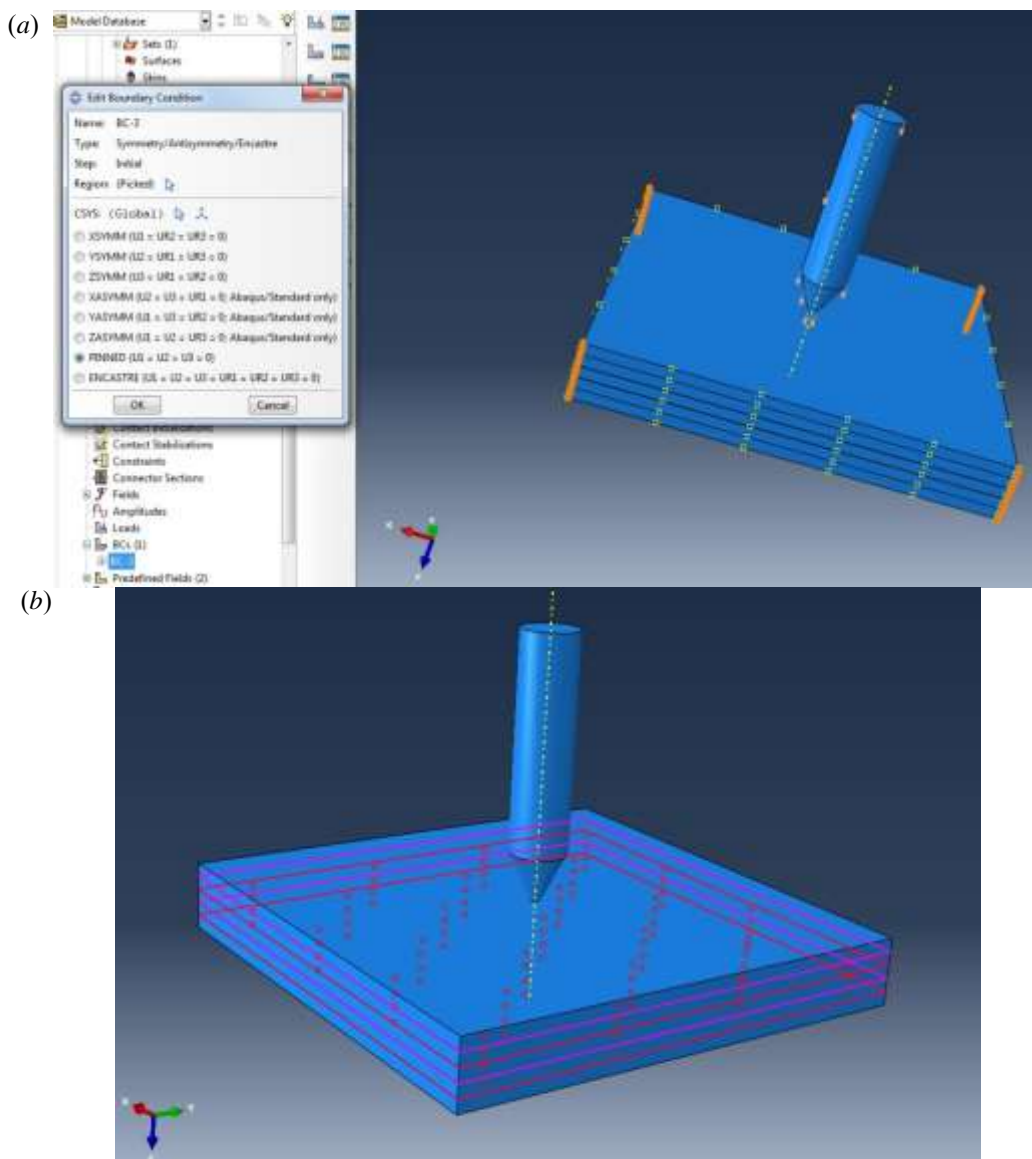

Fig. 15 3D FE model of projectile and composite shield configuration made of homogenous layers: (a) boundary conditions (b) dynamic friction interaction boundary.

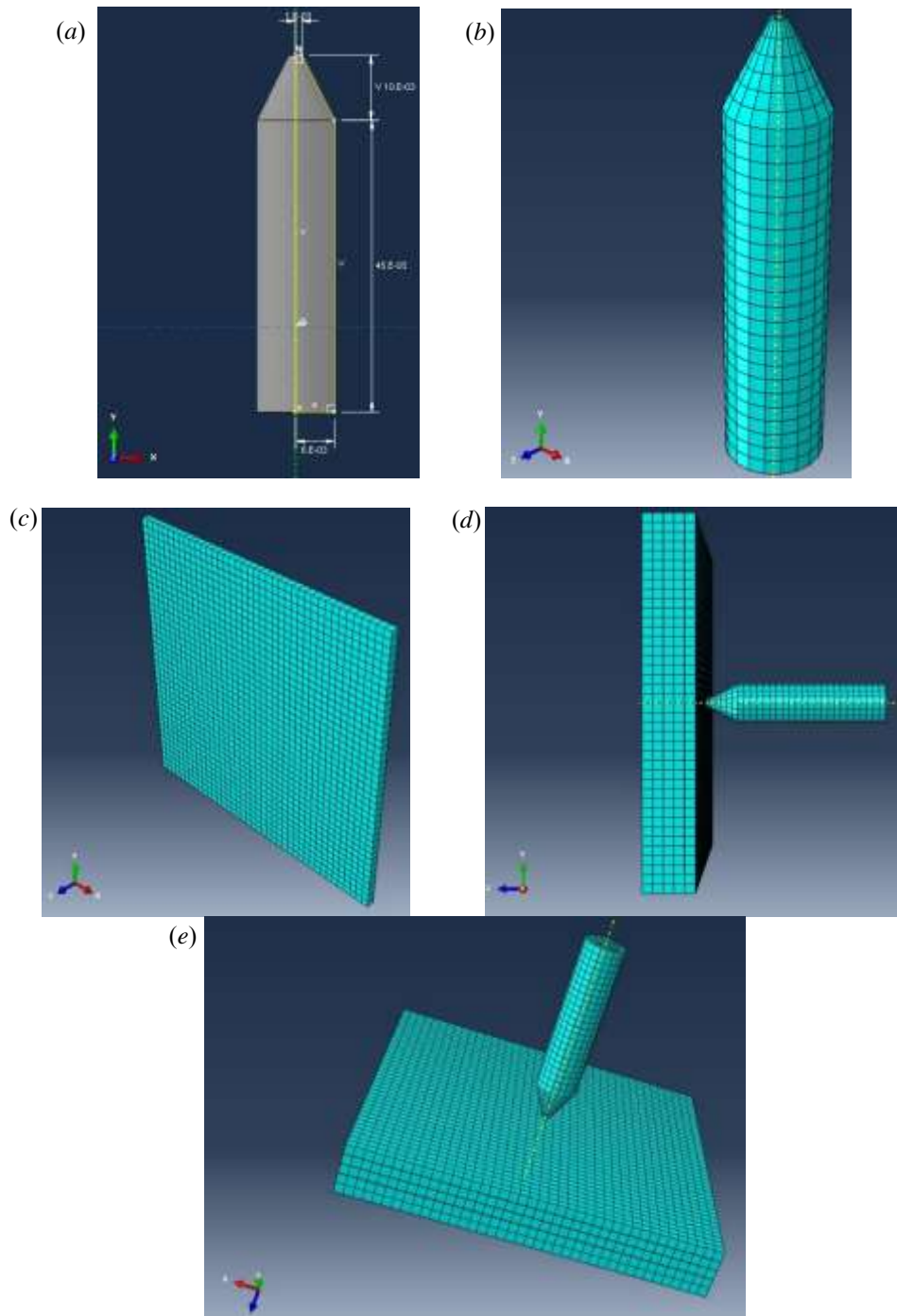Fig. 16 3D FE model of projectile and composite shield configuration made of homogenous layers: (*a*) projectile geometry (*b*) projectile FE meshing (*c*) single plate meshing (*d*) side view of assembly meshing (e) isometry view of assembly meshing.

Jacob Nagler

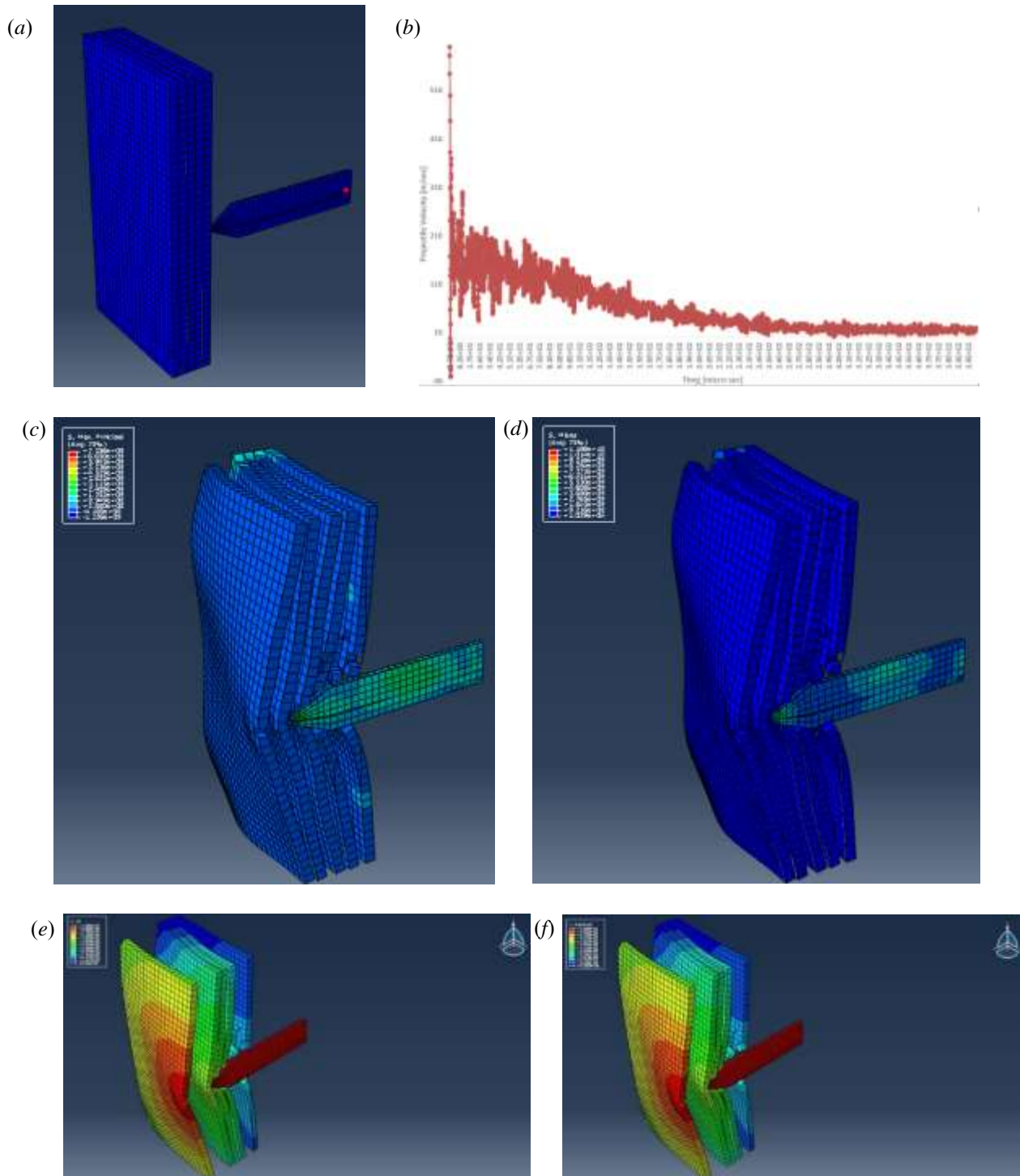Fig. 17 3D FE model of projectile and composite shield configuration made of homogenous layers: (*a*) projectile velocity point of measurement (*b*) projectile FEM velocity behavior (*c*) Maximum principal stress results of 3D FE assembly model (*d*) Von-Mises stress results of 3D FE assembly model (*e*) displacement magnitude results of 3D FE assembly model (*f*) displacement in the *z* axial direction of 3D FE assembly model

Table 1 Armor geometrical properties per B.C., I.C. as input data for the FEM

Physical Property	Value [M.K.S.]
Target geometrical features	Five straight disk plates (layers) with diameter of 72 [mm] and 2.8 [mm] width, respectively. Total width = 14 [mm].
Mechanical loading simulating bullet projectile ballistic penetration	$P(r_i, z = L, t) = H(t) = \begin{cases} t \leq 0: 0\ [Pa] \\ 0 < t \leq 5\ [\mu sec]: 4[GPa] \end{cases}$ $r_i - specific\ radius$ characterized by land diameter of 5.56 [mm] (impact dynamic pressure suits to velocity impact of 1000 m/sec). L – the total shield length. The contact acting area circular diameter equal to 5.56 [mm] and the equivalent total pressure by the projectile is $\frac{\rho}{2}v^2 \approx 4[GPa]$.
Mechanical boundary conditions	$u_{i,t\leq 0} = Free$ $u_{t>0} = Free$
Thermal boundary and initial conditions simulating bullet projectile ballistic penetration	$T(r_i, z = L, t) = H(t) = t \leq 0: -248.15\ [\ ^0C]$ $\left(T\vert_{r,z,t<0}\right)_{i.c.} = -248.15\ [\ ^0C]$
Analysis and element mesh rules details (No., size, type)	**Abaqus**: Type: Axi-symmetric, CAX4RT, Quad. Number of elements: 5400. Element Size: 0.3 [mm] Analysis type: plain – strain. total time = 5 $[\mu sec]$

Table 2 Protective shield components materials properties

Materials	Density	Young's Modulus [GPa]	Poisson's ratio	Longitudinal Sound of velocity	Expansion coefficient	Thermal cond.	Specific heat capacity

Jacob Nagler

	$[kg/m^3]$			$[m/sec]$	$[1/\ ^0K]$	$[W/\ m\ ^0K]$	$[J/kg\ ^0K]$
SiC$_P$	3215	410	0.14	11772	$5.2 \cdot 10^{-5}$	120	750
304 Steel	7850	210	0.33	6160	$1.2 \cdot 10^{-5}$	44.5	440
Al7075-T651	2700	70	0.31	6037	$6.9 \cdot 10^{-5}$	167	910
Kevlar 49	1440	112	0.36	10450	$1.1 \cdot 10^{-8}$	0.04	1420
Graphite (Crystalline)	2250	12	0.3	2335	1.4e-6	2.2	707
Tungsten	15000	255 (shear modulus)	0.28	5200	$2.5 \cdot 10^{-5}$	95	250

Table 3 Armor geometrical properties per B.C., I.C. as input data for the FEM of single isotropic and homogenous versus non-homogenous and non-isotropic layers

Physical Property	Value of single homogenous layer [M.K.S.]	Value of single Non-homogenous layer [M.K.S.]
Target geometrical features	Single straight disk plate (layers) with diameter of 72	Single straight disk plate (layers), containing two rows of

	[mm] and 2.8 [mm] width, respectively.	12 particles each (particle diameter = 0.5 mm), divided uniformly, with diameter of 72 [mm] and 2.8 [mm] width, respectively.
The material configurations	SiCp, Kevlar 49 and Graphite single layers	1. SiCp with Al/Steel/Kevlar 49 particles 2. Kevlar 49 with Al/Steel/Air/Oil/Water particles. 3. Graphite with Al/Steel/Air/Oil/Water particles. All particles have elastic properties due to their enclosed – cell foam shell.
Mechanical boundary conditions for single SiCp layer only	$u_{i,t\leq0} = Free$ $u_{t>0} = Free$ $P(r_i, t) = H(t)$ $= \begin{cases} t \leq 0: 0\ [Pa] \\ 0 < t \leq 5\ [\mu sec]: 4[GPa] \end{cases}$	Same

Thermal boundary and initial conditions for all SiCp, Kevlar and Graphite types of single layers	$T(r_i, z = L, t) = H(t) = t$ $\leq 0: 726.85 \ [\ ^0C]$ $(T\vert_{r,z,t<0})_{i.c.} = -248.15 \ [\ ^0C]$	Same
Analysis and element mesh rules details (No., size, type)	**Abaqus**: Type: Axi-symmetric, CAX4RT, Quad. Number of elements: 1080. Element Size: 0.3 [mm] Analysis type: plain − strain. total time = 5 $[\mu sec]$	Same Number of elements: 9028. Element Size: 0.1 [mm] Same

Table 4 Armor geometrical properties per B.C., I.C. as input data for the FEM selected single non-homogenous and non-isotropic layer under the influence of particle size effects

Physical Property	Value of single Non-homogenous and non-isotropic layer [M.K.S.]
Target geometrical features	Single straight disk plate (layers), containing two rows of 12 particles each, divided uniformly, with diameter of 72 [mm] and 2.8 [mm] width, respectively.
The material configurations	1. SiCp with Kevlar 49 particles. 2. Kevlar 49 with Al particles. The two cases were examined for particle diameter nominal sizes of 0.3, 0.5 and 1*mm*.

Mechanical boundary conditions for single SiCp layer only	$u_{i,t \leq 0} = Free$ $u_{t>0} = Free$ $P(r_i, t) = H(t) = \begin{cases} t \leq 0: 0\ [Pa] \\ 0 < t \leq 5\ [\mu sec]: 4[GPa] \end{cases}$
Thermal boundary and initial conditions for all SiCp and Kevlar types of single layers	$T(r_i, z = L, t) = H(t) = t \leq 0: 726.85\ [\ ^0C]$ $\left(T\vert_{r,z,t<0}\right)_{i.c.} = -248.15\ [\ ^0C]$
Analysis and element mesh rules details (No., size, type)	Type: Axi-symmetric, CAX4RT, Quad. Number of elements (range): 10207-11535, Element Size: 0.1 [mm]. time = 2.5 [μsec]

Table 5 Protective shield components materials plastic properties (Table 2 continuation)

Materials	Density [kg/m^3]	Young's Modulus [GPa]	Poisson's ratio	Longitudinal Sound of velocity [m/sec]	Expansion coefficient [1/ ^0C]	Thermal cond. [$W/m\ ^0C$]	Specific heat capacity [$J/kg\ ^0C$]
SiC$_P$	Material parameters of Abaqus JH2 model:						

ρ_0	G	A	N	B	M	C	$\dot{\epsilon}_0$
3215 kg/m³	193 GPa	0.96	0.65	0.35	1.0	0.009	1.0
T	σ_i^{max}	σ_f^{max}	HEL	p_{HEL}	β		
0.75 GPa	1.24	0.132	11.7 GPa	5.13 GPa	1.0		
D_1	D_2	$\bar{\epsilon}_{f,max}^{pl}$	$\bar{\epsilon}_{f,min}^{pl}$	FS	IDamage		
0.48	0.48	1.2	0.0	0.2	0		
K_1	K_2	K_3					

Johnson – Cook Plastic Parameters:

A = 310[MPa], B = 1 [GPa], n = 0.65, m = 1, $T_{melting} = 1673[K]$, $T_{initial} = 300[K]$,

304 Steel   C=0.07, $\dot{\varepsilon}_0 = 0.1\ [1/sec]$

Ductile damage parameters: $\varepsilon_{fracture} = 0.25$, Stress triaxiality = 1/3, $\dot{\varepsilon}\ =$

100[1/sec], $x_{failure} = 0.25mm$

Johnson – Cook Plastic Parameters:

A = 520[MPa], B = 477 [MPa], n = 0.52, m = 1, $T_{melting} = 893[K]$, $T_{initial} =$

300[K], C=0.001, $\dot{\varepsilon}_0 = 0.0005\ [1/sec]$

Al7075-   Johnson – Cook Damage Parameters:

T651

d1	d2	d3	d4	d5
0.096	0.049	-3.465	0.016	1.099

$x_{failure} = 0.2mm$

Plastic Parameters: $\sigma_Y = 20[MPa]$, $\sigma_{failure} = 500[MPa]$, $\varepsilon_{failure} = 0.025$

Hardening Parameters – Power law Model: $n = 30$, Multiplier = 0.9

Kevlar 49

Ductile damage parameters: $\varepsilon_{fracture} = 0.35$, Stress triaxiality = 0.3, $\dot{\varepsilon}\ =$

100[1/sec], $x_{failure} = 1mm$

| Graphite (Crystalline) | Plastic Parameters: $\sigma_Y = 35[MPa]$, $\sigma_{failure} = 140[MPa]$, $\varepsilon_{failure} = 0.08$ |
| | Ductile damage parameters: $\varepsilon_{fracture} = 0.08$, Stress triaxiality = -1/3, $\dot{\varepsilon} = 100[1/sec]$, $x_{failure} = 0.2mm$ |

Johnson – Cook Plastic Parameters:

A = 3 [GPa], B = 89 [GPa], n = 0.65, m = 1, $T_{melting} = 1768[K]$, $T_{initial} = 300[K]$,

C=0.016, $\dot{\varepsilon}_0 = 1\ [1/sec]$

| Tungsten | Johnson – Cook Damage Parameters: |

d1	d2	d3	d4	d5
0	0.0019	-3	0	0

$$x_{failure} = 0.2mm$$